# Precise Calibration for Biological Acoustic Impedance Microscope

N.Hozumi, A Nakano
Aichi Institute of Technology
Toyota, Japan
hozumi@aitech.ac.jp

S. Terauchi, M. Nagao, S. Yoshida
Toyohashi University of Technology
Toyohashi, Japan

K. Kobayashi
Honda Electronics Co., Ltd.
Toyohashi, Japan

S. Yamamoto
Hamamatsu University School of Medicine
Hamamatsu , Japan

Y. Saijo
Tohoku University
Sendai, Japan

*Abstract*— **This report deals with the scanning acoustic microscope for imaging cross sectional acoustic impedance of biological soft tissues. A focused acoustic beam with a wide frequency range up to about 100 MHz was transmitted to the tissue object in contact with the "rear surface" of plastic substrate. The reflected signals from the target and reference are interpreted into local acoustic impedance. Two-dimensional profile is obtained by scanning the transducer. As the incidence is not vertical, not only longitudinal wave but also transversal wave is generated in the substrate. The error in estimated acoustic impedance assuming vertical incidence was discussed. The error is not negligible if the angle of focusing is large, or the acoustic impedance of the reference material is far different from the target. However it can be compensated, if the beam pattern and acoustic parameters of coupling medium and substrate were known. The improvement of precision brought by the compensation was ensured by using a droplet of saline solution of which acoustic impedance was known. Finally, a cerebellum tissue of rat was observed with a good precision.**

***Keywords: biological tissue; acoustic impedanc; micro-scale imaging.***

## I. INTRODUCTION

In most optical microscopic observation of biological tissue, the specimen is sliced into several micrometers in thickness, and fixed on a glass substrate. The microscopy is obtained by transmitted light through the specimen. As it is normally not easy to have a good contrast by local difference in refraction and/or transmission spectrum, the specimen is usually stained before being observed. It can be classified as a kind of chemical imaging, since only a portion that has a specific chemical property can be stained by selecting an appropriate staining material. However, the staining has some disadvantages. It normally takes several hours to several days to finish the process. Furthermore, the tissue, after being stained, often completely loses its biological functions. For this reason, observation with staining process is chemically destructive.

On the other hand, acoustic micro-imaging can be performed without staining process. In this sense it is chemically non-destructive. The observation can be finished in a very short time, as it does not need the staining process. It is considered to become a powerful tool for tissue characterization that can image elastic parameters. Most of ultrasonic microscopes are scanning type, in which the response to a focused acoustic signal is successively acquired while the beam is mechanically scanned [1-4]. The authors have recently proposed the acoustic impedance microscope that can image local distribution of cross sectional acoustic impedance of soft tissues [5,6]. In this report, its methodology and improvement for establishing precision of measurement will be described. As an specimen for observation, cerebellar tissue of a rat was observed.

## II. SYSTEM SETUP

Fig. 1 illustrates the outline of the acoustic impedance microscope. Distilled water was used as the coupling medium between the substrate and transducer. The transducer was PVDF-TrFE type. It was 2.4 mm in aperture diameter, and 3.2 mm in focal length, its angle of focusing being 22 deg. The acoustic wave, being focused on the interface between the substrate and tissue, was transmitted and received by the same transducer. The acoustic pulse had a wide frequency range from 10 to 100 MHz. Two-dimensional profile of acoustic im-

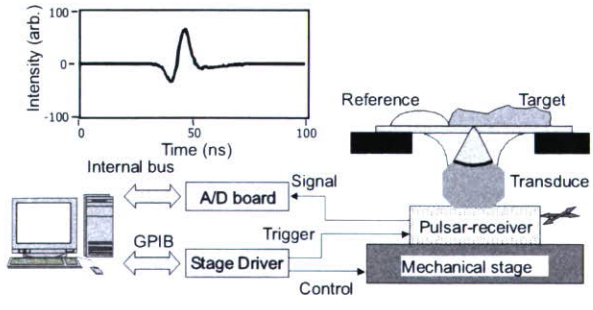


Fig. 1. Schematic diagram of the measurement system and acoustic waveform reflected from the target.

pedance was obtained by mechanically scanning the transducer using the stage driver, maintaining the focal point on the "rear surface" of the substrate. A typical field of view of 2 mm x 2 mm was covered with 200 x 200 pixels. It took typically 1 - 1.5 minutes for one observation. All the measurements were performed at room temperature.

## III. Calibration Assuming Vertical Incidence

As shown in Fig. 2, the signal reflected from the target is compared with that reflected from the reference material. If the incident angle can be approximated to be perpendicular to the substrate, the target signal compared with the reference signal is interpreted into acoustic impedance as;

$$Z_{tgt} = \frac{1+\frac{S_{tgt}}{S_0}}{1-\frac{S_{tgt}}{S_0}} \cdot Z_{sub} = \frac{1-\frac{S_{tgt}}{S_{ref}} \cdot \frac{Z_{sub}-Z_{ref}}{Z_{sub}+Z_{ref}}}{1+\frac{S_{tgt}}{S_{ref}} \cdot \frac{Z_{sub}-Z_{ref}}{Z_{sub}+Z_{ref}}} \cdot Z_{sub} \quad (1),$$

where $S_0$ is the transmitted signal, $S_{tgt}$ and $S_{ref}$ are reflections from the target and reference, $Z_{tgt}$ , $Z_{ref}$ and $Z_{sub}$ are the acoustic impedances of the target, reference and substrate, respectively [5]. As for the substrate, polystyrene dish ($Z_{sub}$ =2.46 MNs/m$^3$) with 0.8 mm in thickness was chosen, and as for the reference material, either distilled water ($Z_{ref}$ =1.49 MNs/m$^3$) or air ($Z_{ref}$ =0.4 kNs/m$^3$) was employed.

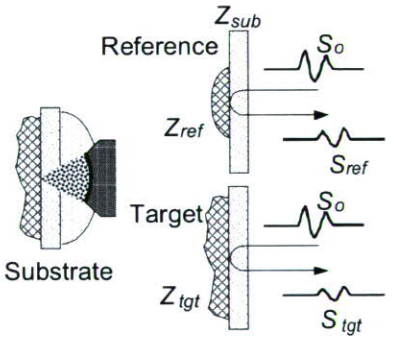


Fig. 2. Illustration for calibration of the acoustic impedance.

## IV. Oblique Incidence

The estimation of acoustic impedance based on eq.(1) assumes that a plane wave is transmitted onto the target, although in fact the acoustic beam has a finite angle of focusing as shown in Fig. 3. The apparent reflection constant at the target may be different from that calculated by eq. (1), when the angle of focusing is large. In addition, when the incident angle is not zero, a part of longitudinal wave may be converted into transversal wave. This may bring an additional error in estimation of the acoustic impedance. For these reasons, error estimation was performed.

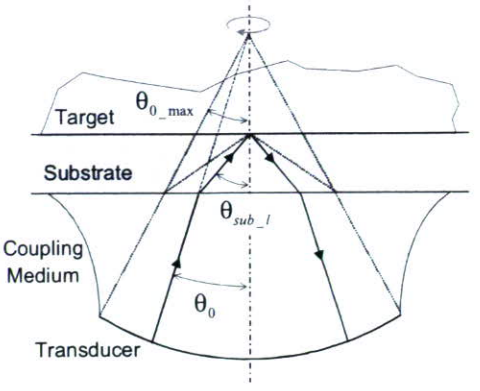


Fig. 3. Illustration of focused acoustic beam.

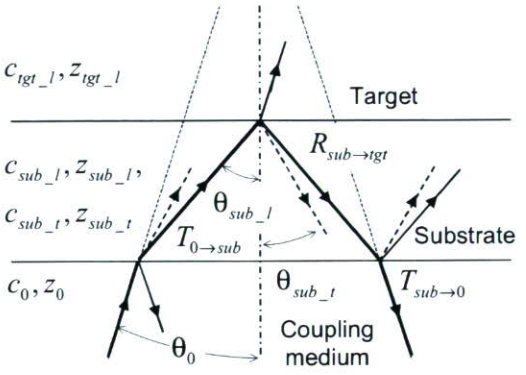


Fig. 4. Propagation of the acoustic wave with an incident angle $\theta_0$. Solid and broken lines represent longitudinal and transversal waves, respectively. Z and c represent acoustic impedance and sound speed. l and t in the suffix indicate longitudinal and transversal waves.

Figure 4 illustrates the propagation of an acoustic wave with an incident angle of $\theta_0$. The direction of the longitudinal wave propagating through the substrate obeys the Snell's law as;

$$\theta_{sub\_l}(\theta_0) = \sin^{-1}\left(\frac{c_{sub\_l}}{c_0}\sin\theta_0\right) \quad (2).$$

As is seen in the figure, three transversal waves are generated before the echo comes back to the transducer. These affect the apparent reflectance, however, as their sound speed is different from that of the longitudinal wave, they are not received in the limited width of the time-window.

In this report, it is assumed that transversal wave can propagate neither in the soft tissue nor the reference material. Subsequently, on the "rear surface", three modes of waves, transmitted longitudinal, reflected longitudinal and reflected transversal, are generated by the incident longitudinal wave. The reflection constant (ratio of reflected longitudinal and incident longitudinal) at the "rear surface" is represented as;

$$R_{sub\to tgt}(Z_{sub\_l}, c_{sub\_l}, c_{sub\_t}, Z_{tgt}, c_{tgt}, \theta_0)$$
$$= \frac{M_{sub} - \cos^2(2\theta_{sub\_t}) + N_{sub\to tgt}}{M_{sub} + \cos^2(2\theta_{sub\_t}) + N_{sub\to tgt}}$$

$$\theta_{sub\_t} = \sin^{-1}\left(\frac{c_{sub\_t}}{c_{sub\_l}} \sin\theta_{sub\_l}\right),$$

$$M_{sub} = \left(\frac{c_{sub\_t}}{c_{sub\_l}}\right)^2 \sin\theta_{sub\_t} \sin\theta_{sub\_l},$$

$$N_{sub\to tgt} = \frac{Z_{tgt}\cos\theta_{sub\_l}}{Z_{sub\_l}\cos\theta_{tgt}},$$

$$\theta_{tgt} = \sin^{-1}\left(\frac{c_{tgt}}{c_{sub\_l}} \sin\theta_{sub\_l}\right) \quad (3).$$

Transmission of the longitudinal wave through the "front surface" takes place twice, and affects the apparent reflection constant as;

$$T_{0\to sub} \cdot T_{sub\to 0} = T'_{0\to sub}(Z_0, c_0, Z_{sub\_l}, c_{sub\_l}, c_{sub\_t}, \theta_0)$$
$$= \frac{4N_{0\to sub}\cos^2(2\theta_{sub\_t})}{\left\{M_{sub} + \cos^2(2\theta_{sub\_t}) + N_{0\to sub}\right\}^2}$$

$$N_{0\to sub} = \frac{Z_0 \cos\theta_{sub\_l}}{Z_{sub\_l}\cos\theta_0} \quad (4).$$

Assuming that the aberration is negligible, the apparent reflection constant (ratio of received and sent waves) is described as;

$$S_{tgt}(Z_{tgt}, c_{tgt}, \theta_{0\_max}) / S_0$$
$$= \frac{\int_0^{\theta_{0\_max}} 2\pi L^2 \sin\theta_0 R_{sub\to tgt}(\theta_0) T'_{0\to sub}(\theta_0) d\theta_0}{\int_0^{\theta_{0\_max}} 2\pi L^2 \sin\theta_0 d\theta_0} \quad (5),$$

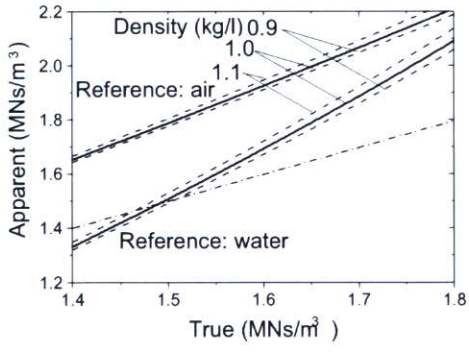


Fig. 5. Relation between true and apparent values of acoustic impedance. Angle of focusing: 22 deg. $Z_{sub\_l}$=2.46 MNs/m$^3$, $c_{sub\_l}$=2.34 km/s, $c_{sub\_t}$=1.15 km/s.

where L is the focal length in the coupling medium.

The reflected signal from the reference material is calculated in the same manner as $S_{ref}(Z_{ref}, c_{ref}, \theta_{0\_max}) / S_0$. Referring to eq. (1), the apparent acoustic impedance assuming vertical incidence is estimated as;

$$Z_{tgt\_app} = \frac{1 + \frac{S_{tgt}(Z_{tgt}, c_{tgt}, \theta_{0\_max})}{S_{ref}(Z_{ref}, c_{ref}, \theta_{0\_max})} \cdot \frac{Z_{ref} - Z_{sub\_l}}{Z_{ref} + Z_{sub\_l}}}{1 - \frac{S_{tgt}(Z_{tgt}, c_{tgt}, \theta_{0\_max})}{S_{ref}(Z_{ref}, c_{ref}, \theta_{0\_max})} \cdot \frac{Z_{ref} - Z_{sub\_l}}{Z_{ref} + Z_{sub\_l}}} \cdot Z_{sub\_l} \quad (6).$$

Figure 5 shows the relation between the "true" and "apparent" values of acoustic impedance. As the result is dependent on $c_{tgt}$, it is parameterized by the density, which is given by $Z_{tgt}$ / $c_{tgt}$. The true and apparent values coincide when $Z_{tgt}$=$Z_{ref}$ =1.49 MNs/m (calibrated by water), and the gap increases as $Z_{tgt}$ becomes distant from $Z_{ref}$. Using the air as the reference brings more significant gap, as its acoustic impedance is far more distant from the tissue. As the acoustic impedance of soft tissue is distributed approximately between 1.4 and 1.7 MNs/m$^3$, the error gap with these conditions is not negligible. On the other hand, the apparent value does not significantly change even if the density changes from 0.9 to 1.1 kg/*l*, in which the value of soft tissues is distributed.

## V. Compensation

The apparent acoustic impedance calibrated by using eq. (1) can be compensated by the curves shown in Fig. 5. In order to ensure the improvement of precision brought by the above compensation, droplets of saline solution were observed. The acoustic impedance of these droplets were once estimated by

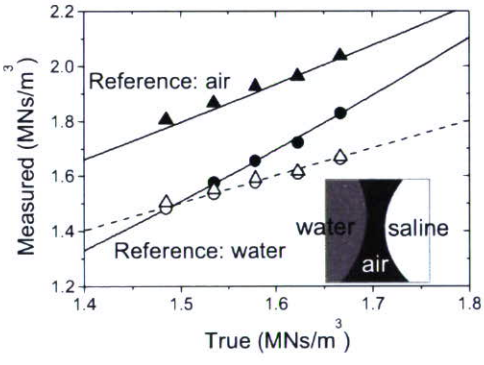


Fig. 6. Result of measurement for droplets of saline solution. True value, corresponding to salinity, is taken from the database. Filled plots indicate values as calibrated assuming vertical incidence, and open plots indicate values after the compensation considering oblique incidence. Solid lines correspond to those in Fig. 5. Angle of focusing: 22 deg. $Z_{sub\_l}$=2.46 MNs/m$^3$, $c_{sub\_l}$=2.34 km/s, $c_{sub\_t}$=1.15 km/s. Assumed density: 1.0 kg/*l*.

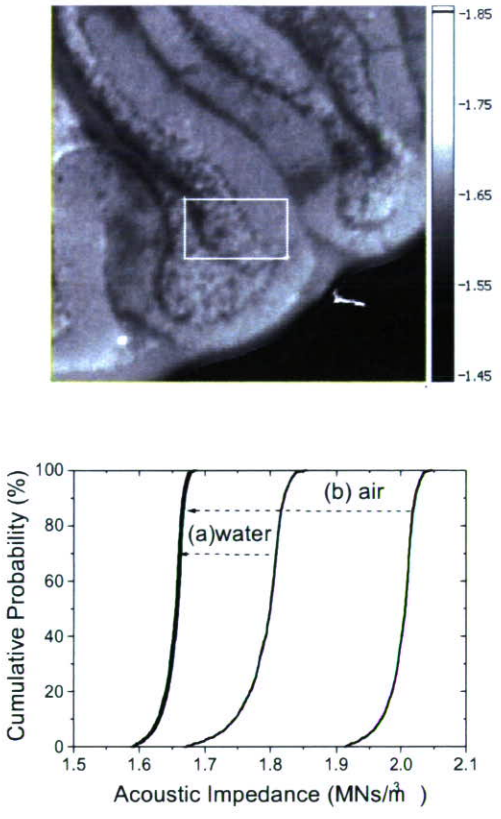


Fig. 7. Acoustic impedance micro-image of a cerebellar tissue of a rat (indicated in MNs/m$^3$, 2 mm x 2 mm) and cumulative probability of acoustic impedance in the region indicated as the white square, before and after the compensation: (a) calibrated by distilled water ($Z_{ref}$=1.49 MNs/m$^3$, $c_{ref}$=1.49 km/s), (b) calibrated by air ($Z_{ref}$=0.4 kNs/m$^3$, $c_{ref}$=0.34 km/s).

assuming vertical incidence, using either distilled water or the air as a reference. As the acoustic impedance of these saline droplets depending on salinity is known, these values were assumed to be the "true" values. As shown in Fig. 6, the measured value depends on the reference material and whether or not the compensation is performed. It is seen that the calibrated values assuming vertical incidence agree with the "apparent values" in Fig. 5. The value calibrated by air is more distant from the true value. The value calibrated by water is the same as the true value when the target is identical to the reference, and becomes more distant from the true value as the target becomes more different from the reference. The values after the compensation is very close to the true value, not depending on the reference material.

The acoustic impedance image of a cerebellar tissue of a rat shown in Fig. 7 was obtained after the compensation. In this report, the density was approximated to be 1.0 kg/*l*. Note that the tissue was chemically fixed using formaldehyde, so the value might be a bit higher than the fresh one. The graph for cumulative probability in Fig. 7 shows the distribution of acoustic impedance in the region surrounded by the white square in the micro-image. The compensated value is distributed between 1.59 and 1.68 MNs/m$^3$, regardless of the reference material. Before the compensation, it used to be distributed between 1.68 and 1.85 MNs/m$^3$ when calibrated by distilled water, and between 1.92 and 2.04 MNs/m$^3$ when calibrated by air. The result that the distributions after the compensation agree quit well suggests the adequacy of the compensation.

## VI. Conclusions

Acoustic impedance microscope for biological soft tissues is proposed. Cross-sectional profile of the acoustic impedance of the tissue is obtained by mechanically scanning the transducer. The value calibrated assuming vertical incidence was considered to have non-negligible error when the angle of focusing was as large as 22 deg. The error, however, can be compensated by calculating reflection and transmission coefficients depending on the incident angle of each wave component. The observation of cerebellum tissue of a rat proved the adequacy of the compensation.

## Acknowledgements

This study was financially supported by Grants-in-Aid for Scientific Research, and Japan Society for the Promotion of Science and Health and Labor Sciences Research Grants from the Ministry of Health, Labor and Welfare for the Research on Advanced Medical Technology.

## References

[1] Y. Saijo, M. Tanaka, H. Okawai, H. Sasaki, S. Nitta & F. Dunn: "Ultrasonic Tissue Characterization of Infarcted Myocadium by Scanning Acoustic Microscopy", *Ultrasound in Med. & Biol.*, 23-1, 77 (1997).

[2] H. Okawai, K Kobayashi & S. Nitta: "An Approach to Acoustic Properties of Biological Tissues Using Acoustic Microgfraphs of Attenuation Constant and Sound Speed", *J. Ultrasound Med.*, 20, 891 (2001).

[3] N. Hozumi, R. Yamashita, C-K Lee, M. Nagao, K. Kobayashi, Y. Saijo, M. Tanaka, N. Tanaka & S Ohtsuki: "Ultrasonic Sound Speed Microscope for Biological Tissue Characterization Driven by Nanosecond Pulse", *Acoustic Science & Technology*, 24, 386 (2003).

[4] N. Hozumi, R. Yamashita, C-K. Lee, M. Nagao, K. Kobayashi, Y. Saijo, M. Tanaka, N. Tanaka & S.Ohtsuki: "Time –frequency analysis for pulse driven ultrasonic microscopy for biological tissue characterization", *Ultrasonics*, 42, 717 (2003).

[5] N. Hozumi, A. Kimura, S. Terauchi, M. Nagao, S. Yoshida, K. Kobayashi & Y. Saijo: "Acoustic Impedance Micro-imaging for Biological Tissue Using a Focused Acoustic Pluse with a Frequency Range Up to 100 MHz", *Proc. IEEE International Ultrasonics Symposium*, 170-173 (2005).

[6] A. Kimura, N. Hozumi, S. Terauchi, M. Nagao, S. Yoshida, K. Kobayashi & Y. Saijo: "Development of Cerebella Tissue of Rat Characterized by Acoustic Impedance Microscope", *Proc. IEEE International Ultrasonics Symposium*, 423-426 (2006).

*The American Journal of Pathology, Vol. 171, No. 4, October 2007*

*DOI: 10.2353/ajpath.2007.061191*

*Cardiovascular, Pulmonary and Renal Pathology*

# Macrophage Colony-Stimulating Factor Improves Cardiac Function after Ischemic Injury by Inducing Vascular Endothelial Growth Factor Production and Survival of Cardiomyocytes

Tatsuma Okazaki,* Satoru Ebihara,* Masanori Asada,* Shinsuke Yamanda,* Yoshifumi Saijo,† Yasuyuki Shiraishi,† Takae Ebihara,* Kaijun Niu,* He Mei,* Hiroyuki Arai,* and Tomoyuki Yambe†

*From the Department of Geriatrics and Gerontology,* Tohoku University School of Medicine, Sendai; and the Department of Medical Engineering and Cardiology,† Institute of Development, Aging, and Cancer, Tohoku University, Sendai, Japan*

**Macrophage colony-stimulating factor (M-CSF), known as a hematopoietic growth factor, induces vascular endothelial growth factor (VEGF) production from skeletal muscles. However, the effects of M-CSF on cardiomyocytes have not been reported. Here, we show M-CSF increases VEGF production from cardiomyocytes, protects cardiomyocytes and myotubes from cell death, and improves cardiac function after ischemic injury. In mice, M-CSF increased VEGF production in hearts and in freshly isolated cardiomyocytes, which showed M-CSF receptor expression. In rat cell line H9c2 cardiomyocytes and myotubes, M-CSF induced VEGF production via the Akt signaling pathway, and M-CSF pretreatment protected these cells from $H_2O_2$-induced cell death. M-CSF activated Akt and extracellular signal-regulated kinase signaling pathways and up-regulated downstream anti-apoptotic Bcl-xL expression in these cells. Using goats as a large animal model of myocardial infarction, we found that M-CSF treatment after the onset of myocardial infarction by permanent coronary artery ligation promoted angiogenesis in ischemic hearts but did not reduce the infarct area. M-CSF pretreatment of the goat myocardial infarction model by coronary artery occlusion-reperfusion improved cardiac function, as assessed by hemodynamic parameters and echocardiography. These results suggest M-CSF might be a novel therapeutic agent for ischemic heart disease. *(Am J Pathol 2007, 171:1093–1103; DOI: 10.2353/ajpath.2007.061191)***

The administration of angiogenic growth factors such as vascular endothelial growth factor (VEGF) is an innovative strategy to treat myocardial ischemia. VEGF has been used in animal models and in clinical trials of myocardial ischemia to develop growth of collateral blood vessels and to promote myocardial perfusion, and its therapeutic potential has been reported.[1–3] Hematopoietic growth factors are potent therapeutic agents for myocardial infarction. Erythropoietin improved cardiac function after myocardial infarction.[4,5] Granulocyte colony-stimulating factor (G-CSF) improved cardiac function and prevented cardiac remodeling after myocardial infarction.[6] A combination of stem cell factor and G-CSF treatment improved cardiac function and survival after myocardial infarction.[7] Macrophage colony-stimulating factor (M-CSF) in combination with G-CSF improved ventricular function after myocardial infarction in rats, but few results were shown by M-CSF treatment alone, and their mechanism was not defined.[8] Moreover, to estimate growth factor-induced therapeutic angiogenesis in hearts, large animal models are necessary,[3] but the effects of M-CSF in large animal models have not been reported. M-CSF has been initially characterized as a hematopoietic growth factor, and has been used to prevent severe infections in myelosuppressed patients after cancer chemotherapy.[9,10] M-CSF stimulates the survival, prolifera-

Supported by the Ministry of Education, Science, and Culture (grants 15590795, 18014004, 17590777, and 18790528); the Ministry of Health, Labor, and Welfare of the Japanese Government (Grant for Longevity Science grants 16C-1 and 18C-7); and by the Program for Promotion of Fundamental Studies in Health Science of Organizing for Drug ADR Relief, R&D Promotion, and Product Review of Japan.

Accepted for publication June 27, 2007.

Current address of T.O.: Department of Anatomy, University of California–San Francisco, San Francisco, CA.

Address reprint requests to Satoru Ebihara, M.D., Ph.D., Department of Geriatrics and Gerontology, Tohoku University School of Medicine, Seiryo-machi 1-1, Aoba-ku, Sendai 980-8574, Japan. E-mail: s_ebihara@geriat.med.tohoku.ac.jp.

tion, and differentiation of cells from mononuclear phagocyte lineage.[11]

Expression of VEGF in the heart has been documented,[12,13] and cardiomyocytes have been reported as a major source of VEGF in the heart.[12] Skeletal muscles expressed VEGF,[13,14] and M-CSF increased VEGF production from skeletal muscles *in vivo* and *in vitro*,[14] but it is unknown whether M-CSF increases VEGF production from cardiomyocytes. M-CSF treatment increased serum VEGF levels in mice,[14] and the level was in the potentially therapeutic range that could treat ischemic diseases in human patients.[15]

Erythropoietin and G-CSF directly protected cardiomyocytes from cell death stimulation.[4,6] M-CSF improves the survival of mononuclear phagocyte lineage cells,[11] but the cell survival effect of M-CSF on cardiomyocytes is unknown. As for their signaling pathways, M-CSF activates Akt, extracellular signal-regulated kinase (ERK), and/or Janus-associated kinase (Jak)-signal transducer and activator of transcription (STAT) cell signaling pathways in bone marrow-derived macrophages and macrophage cell lines.[16–18] M-CSF increased VEGF production in skeletal muscles via Akt activation *in vitro*.[14] However, the cell signaling pathways of M-CSF in cardiomyocytes have not been investigated.

In the present study, we investigated the angiogenic and protective effects of M-CSF on cardiomyocytes *in vitro* and *in vivo*, in mice, rats, and goats. We show that M-CSF increases VEGF production in cardiomyocytes via Akt activation, directly protects cultured cardiomyocytes and myotubes from cell death stimulation by Akt and ERK activation and by up-regulation of downstream anti-apoptotic protein Bcl-xL. Moreover, we show the benefits of M-CSF treatment for ischemic heart diseases *in vivo* using goats as a large animal model.

## Materials and Methods

### Reagents and Cell Culture

Human M-CSF (Kyowa Hakko Kogyo, Tokyo, Japan) was dissolved in saline for goat experiments described below or in phosphate-buffered saline (PBS) for other experiments. Phycoerythrin-labeled anti-M-CSF receptor (M-CSF-R) monoclonal antibody, control rat IgG2a, and unlabeled anti-CD16/32 monoclonal antibody were purchased from eBioscience (San Diego, CA). H9c2 cells (American Type Culture Collection, Manassas, VA) were cultured in high-glucose Dulbecco's modified Eagle's medium containing 10% fetal calf serum, 100 U/ml penicillin, and 0.1 mg/ml streptomycin (growth medium, GM). To induce cardiac differentiation, H9c2 myoblasts were cultured in differentiation medium (DM) with daily supplementation of 10 nmol/L *all-trans*-retinoic acid (ATRA) (Sigma, St. Louis, MO), with medium changed every 2 days.[19] The difference between GM and DM is 1% fetal calf serum in DM. H9c2 myoblasts were differentiated to myotubes by culturing in the same DM for 11 days.[20] Mouse primary cardiomyocytes were obtained from 1- to 3-day-old neonatal C57BL/6 mice.[21] Heart ventricles were washed in ice-cold Hanks' balanced salt solution without either $Ca^{2+}$ or $Mg^{2+}$ and then minced. The cells were dissociated with 0.25% trypsin in Hanks' balanced salt solution. The supernatants were collected every 15 minutes and centrifuged. To exclude nonmuscle cells, the cells were cultured at 37°C for 2 hours. Then the suspended cells were collected and cultured at $1 \times 10^5$ cells/cm$^2$. After 48 hours, more than 90% of the cells were considered as cardiomyocytes by cross-striation structure staining with Bodipy FL phallacidin (Molecular Probes, Eugene, OR).

### Cell Proliferation and Cell Death Assays

H9c2 cells ($5 \times 10^3$ cells) were plated on 96-well plates and differentiated to cardiomyocytes or myotubes, and the assays were performed as previously shown.[22] For proliferation assays, H9c2 cardiomyocytes or myotubes were treated with M-CSF for indicated time periods, and the cell numbers were counted by a water-soluble tetrazolium (WST) assay using a cell counting kit (Dojindo, Tokyo, Japan). For cell death assays, differentiated H9c2 cells were incubated with M-CSF in the presence or absence of PD98059 (at 30 or 6 μmol/L; Biosource, Camarillo, CA) or LY294002 (at 10 or 2 μmol/L; Biosource) for 24 hours. Then the cells were stimulated with indicated amount of $H_2O_2$ for 8 hours. The cell viability was determined by the WST assay.

### Flow Cytometry

The cells were incubated with unlabeled anti-CD16/32 monoclonal antibody to block nonspecific binding and then with phycoerythrin-labeled antibodies. Flow cytometry was performed with a FACScan (BD Bioscience, San Jose, CA).[14]

### Histology

The goat hearts were fixed in 10% formalin, embedded in paraffin, and sectioned. The sections were stained with hematoxylin and eosin (H&E) or Masson's elastic stain. The microvessel density in myocardial infarction lesions was determined as previously shown by immunohistochemical staining of goat hearts with polyclonal rabbit anti-human factor VIII-related antigen antibody (DakoCytomation, Carpinteria, CA) at 1:200 dilution.[14,23] The applicability of this antibody to goats was previously reported.[24] The image with the highest microvessel density was chosen at ×100 magnification, and the vessels were counted at ×200 magnification. Two independent investigators counted at least four fields for each section, and the highest count was taken. To quantify the infarct area, a standard point-counting technique was used as previously described with minor modifications.[25] In brief, the whole heart cross section with highest infarct area was selected, and a 200-point grid was superimposed onto each captured image using Adobe Photoshop (Adobe Systems Inc., San Jose, CA). The area fraction of infarction was

calculated by dividing the number of infarct points by the total number of points falling on the tissue section and was expressed as a percentage.

### *Western Blot Analysis*

Western blot analysis was performed as shown previously.[26] H9c2 myoblasts ($5 \times 10^6$ cells) were cultured in GM on day 0. From day 1, the cells were differentiated to cardiomyocytes or myotubes. After differentiation, the cells were serum-starved for 6 hours and stimulated with M-CSF. For inhibitor experiments, the cells were cultured with inhibitors for 30 minutes and then stimulated with M-CSF and inhibitors. PD98059 was incubated at a concentration of 30 or 6 μmol/L, and LY294002 was incubated at a concentration of 10 or 2 μmol/L. The cell lysates were subjected to 12% sodium dodecyl sulfate-polyacrylamide gel electrophoresis and transferred onto polyvinylidene difluoride membranes (Millipore, Billerica, MA). The membranes were blotted with antibodies to phospho-ERK, phospho-Akt, phospho-Stat1, phospho-Stat3, phospho-Bad, Bcl-xL (Cell Signaling Technology, Beverly, MA), phospho-Jak1, or M-CSF-R (Santa Cruz Biotechnology, Santa Cruz, CA). The membranes blotted with antibodies to detect phosphorylation were then reblotted with antibodies to total ERK, Akt, Stat1, Stat3, Bad (Cell Signaling Technology), or Jak1 (Santa Cruz Biotechnology).

### *Mouse and Goat Preparation*

The Laboratory Animal Committee at Tohoku University approved all animal experiments. Male C57BL/6 mice, 7 to 9 weeks old, were injected intramuscularly with M-CSF (200 μg/kg body weight) or PBS (control) for 3 consecutive days ($n = 5$ per group). Adult male goats (48 to 53 kg body weight) were intubated and anesthetized with 2% halothane as previously reported ($n = 3$ per group).[27] The goats were incised between the fourth and fifth ribs, and a left lateral thoracotomy was performed. Myocardial infarction was induced by left anterior descending coronary artery ligation with some modifications.[28] For the permanent left anterior descending coronary artery ligation model, left anterior descending coronary artery was ligated at a point ~60% from the beginning of the left coronary artery to the apex. M-CSF (40 μg/kg body weight) intravenous injection began just after the ligation and continued daily for 13 days; on day 14, the goats were anesthetized with 2% halothane and sacrificed. Control goats were injected with saline. For the ischemia-reperfusion model, M-CSF was injected intravenously for 3 consecutive days. Then the left anterior descending coronary artery was ligated at a point ~40% from the beginning of the left coronary artery to the apex for 30 minutes followed by reperfusion.[5] A micromanometer tipped catheter (Millar Instruments Inc., Houston, TX) was positioned in the left ventricle (LV). Hemodynamic parameters were recorded using a data recording unit (TEAC Corp., Tokyo, Japan) with sampling frequency of 1.5 kHz. Echocardiography was performed using a Sonos 5500 (Hewlett Packard, Andover, MA).

### *Enzyme-Linked Immunosorbent Assay (ELISA)*

Mouse hearts were isolated, washed, homogenized in ice-cold PBS, and centrifuged. The protein level in the supernatant was adjusted to 10 mg/ml by the BCA protein assay kit (Pierce, Rockford, IL), and subjected to ELISA using a VEGF ELISA kit (R&D Systems, Minneapolis, MN). Carrageenan (Sigma) and rat anti-mouse CD11b monoclonal antibody (Serotec, Oxford, UK) treatment was performed as previously reported.[14] Culture medium of mouse primary cardiomyocytes ($2 \times 10^5$ cells) was changed daily. H9c2 myoblasts ($5 \times 10^3$ cells) were differentiated to cardiomyocytes or myotubes. H9c2 cardiomyocytes were incubated with M-CSF and ATRA in the presence or absence of LY294002 (10 μmol/L) for indicated time periods with daily culture medium change. H9c2 myotubes were cultured with M-CSF for indicated time periods. All of the supernatants were assayed by ELISA.

### *RNA Isolation and Reverse Transcriptase-Polymerase Chain Reaction (RT-PCR)*

Total RNA was isolated using RNAzol B reagent (Tel-Test, Friendswood, TX). Placenta total RNA was purchased from BD Biosciences. Quantitative RT-PCR for VEGF and conventional RT-PCR for M-CSF-R were performed as previously shown.[14]

### *Data Analysis*

Data are presented as mean ± SD. Statistical analysis was performed using analysis of variance with Fisher's least significant difference test. $P$ values $<0.05$ were considered as significant.

## *Results*

### *M-CSF Increases Heart VEGF Production* in Vivo

Previous studies have shown that M-CSF increased VEGF production in skeletal muscles, and the heart expresses VEGF. Therefore, we examined whether M-CSF increases heart VEGF production. Mice were treated with M-CSF, and then the cytoplasmic RNA in heart was assessed by quantitative RT-PCR. M-CSF significantly increased VEGF mRNA expression level in the hearts by 221% (Figure 1A). M-CSF receptor (M-CSF-R) mRNA expression was confirmed by conventional RT-PCR, and placenta-derived mRNA was used as a positive control (Figure 1B). To confirm VEGF at the protein level, M-CSF was injected into mice. The hearts were isolated, and ELISA for VEGF was performed. VEGF was detected in controls (Figure 1C). M-CSF significantly increased VEGF in the hearts by 21% (Figure 1C). Because M-CSF induces VEGF production *in vitro* from human monocytes,[29] we sought to clarify whether cardiomyocytes or the monocytes/macrophages in the heart produced VEGF after M-CSF treatment. Mice were treated with carra-

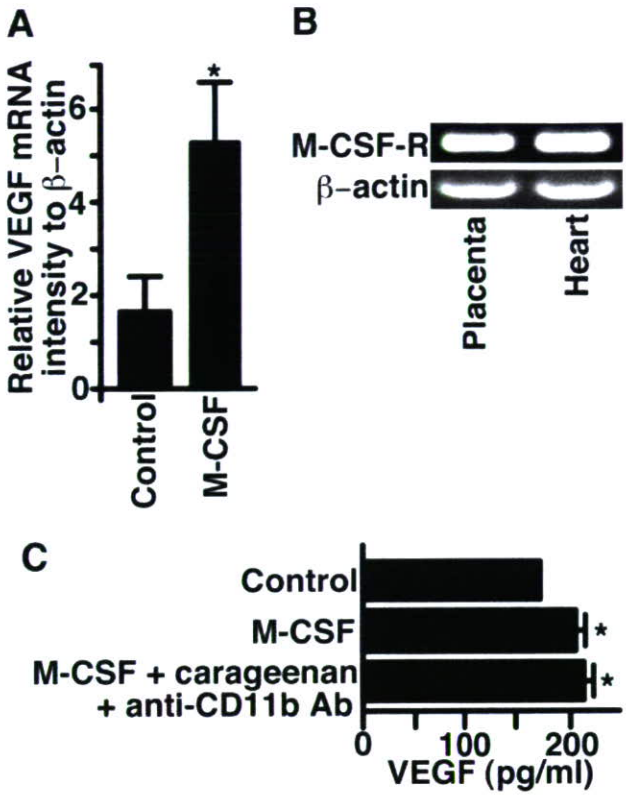


**Figure 1.** M-CSF increased heart VEGF production *in vivo*. Mice were injected intramuscularly with M-CSF (200 μg/kg) or PBS (control) for 3 consecutive days ($n$ = 5 per group). **A:** Quantitative RT-PCR determined the VEGF mRNA expression. M-CSF treatment significantly increased the VEGF mRNA expression in hearts ($^*P < 0.05$). **B:** Conventional RT-PCR determined the M-CSF receptor (M-CSF-R) expression (top), and β-actin expression (bottom). **C:** The hearts were washed, homogenized in PBS, and centrifuged. ELISA determined the VEGF level in the supernatants containing 10 mg/ml protein. M-CSF significantly increased the VEGF level. M-CSF + carrageenan + anti-CD11b Ab indicates mice injected with carrageenin (1 mg) on days 1 and 4, with anti-CD11b monoclonal antibody (0.5 mg) on days 3 and 5, and with M-CSF on days 3, 4, and 5. On day 6, the hearts were isolated. This treatment did not affect the VEGF level ($^*P < 0.05$). Similar results were obtained from two independent experiments.

geenan and anti-CD11b monoclonal antibody to eliminate the monocytes/macrophages, as shown previously.[14] Macrophages were hardly observed in control mice hearts or in treated mice hearts (data not shown). The treatment did not affect M-CSF-induced VEGF production in the heart (Figure 1C).

## *M-CSF Increases VEGF Production by Cardiomyocytes* in Vitro

To confirm the effect of M-CSF on heart VEGF production *in vitro*, mouse neonatal cardiomyocytes were isolated and stimulated with M-CSF. The culture medium was changed daily to maintain cell viability. Control cardiomyocytes produced VEGF, and M-CSF significantly increased the VEGF level on days 2 (by 10%) and 3 (by 31%) (Figure 2A). The M-CSF-R expression on cardiomyocytes was confirmed by fluorescence-activated cell sorting analysis (Figure 2B).

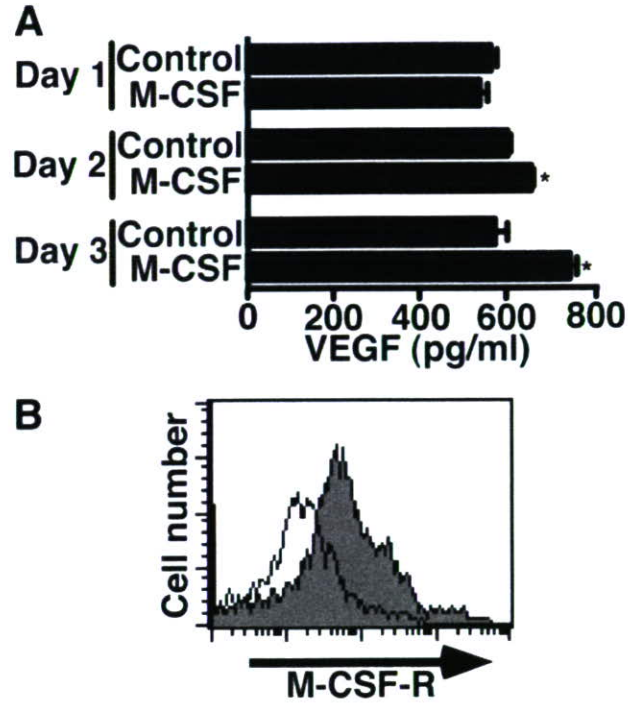


**Figure 2.** M-CSF enhanced heart VEGF production *in vitro*. **A:** Cultured cardiomyocytes from neonatal mice were stimulated with M-CSF (100 ng/ml) for the indicated time periods. Culture medium was changed daily, and the supernatants were subjected to ELISA. M-CSF significantly enhanced VEGF production on days 2 and 3 ($^*P < 0.01$). **B:** Cultured cardiomyocytes from neonatal mice expressed M-CSF-R. The shaded histogram indicates staining with M-CSF-R, and the blank histogram indicates background staining with control IgG. Similar results were obtained from two independent experiments.

## *M-CSF Increases VEGF Production from Differentiated H9c2 Cells*

To investigate the effects of M-CSF on cardiomyocytes more precisely, rat H9c2 myoblast cells were differentiated to cardiomyocytes. H9c2 myoblasts differentiate to cardiomyocytes when they are cultured in DM with ATRA.[19] After differentiation, DM with ATRA was changed daily to maintain cell viability. VEGF was detected in supernatants from controls, and M-CSF increased H9c2 cardiomyocyte VEGF production on days 2 (by 10%) and 3 (by 20%) (Figure 3A). M-CSF increased skeletal muscle VEGF production.[14] H9c2 myoblasts cultured in the DM without ATRA for 11 days differentiate to H9c2 myotubes.[20] After differentiation, H9c2 myotubes were treated with M-CSF. H9c2 myotubes produced VEGF, and M-CSF significantly enhanced VEGF production on day 8 by 29% (Figure 3B).

## *M-CSF Protects Differentiated H9c2 Cells from $H_2O_2$-Induced Cell Death*

Because M-CSF increased VEGF production from differentiated H9c2 cells, we investigated whether M-CSF increased the H9c2 cardiomyocyte cell number and found that it did not (Figure 4A). Similar results were obtained from the H9c2 myotubes (Figure 4A). M-CSF improves the survival of the mononuclear phagocyte lineage

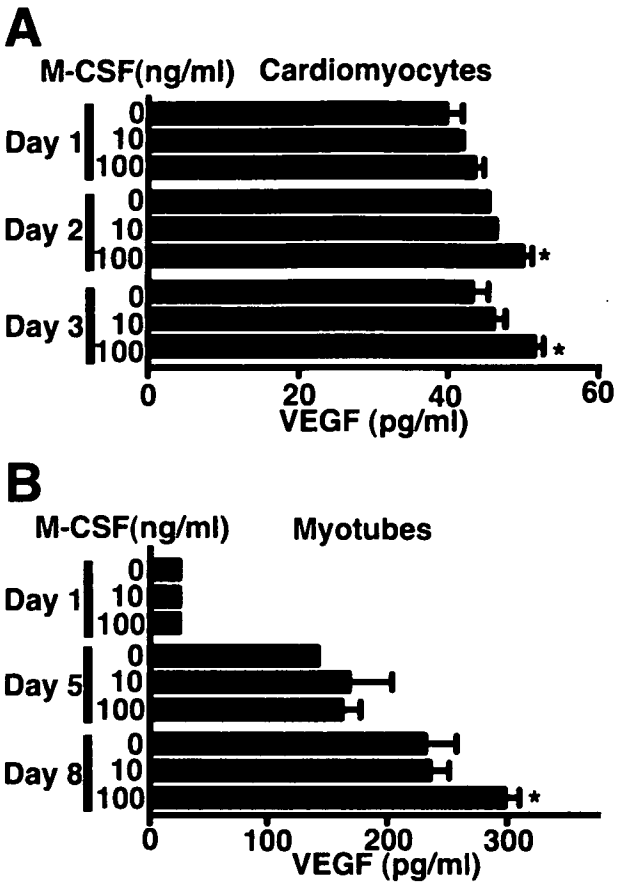


**Figure 3.** M-CSF increased VEGF production in differentiated H9c2 cells. **A:** H9c2 myoblasts cultured in DM (changed every 2 days) with daily supplementation of 10 nmol/L ATRA for 7 days were differentiated to H9c2 cardiomyocytes. The cells were stimulated with the indicated amount of M-CSF for indicated time periods. The culture medium was changed daily, and ELISA determined the VEGF level in the supernatant. M-CSF (100 ng/ml) increased VEGF production on days 2 and 3 ($^*P < 0.05$). **B:** H9c2 myoblasts cultured in the same DM for 11 days were differentiated to H9c2 myotubes. Then the cells were stimulated with the indicated amount of M-CSF for the indicated time periods without medium change. M-CSF (100 ng/ml) significantly increased VEGF production on day 8 ($^*P < 0.03$). Similar results were obtained from three independent experiments.

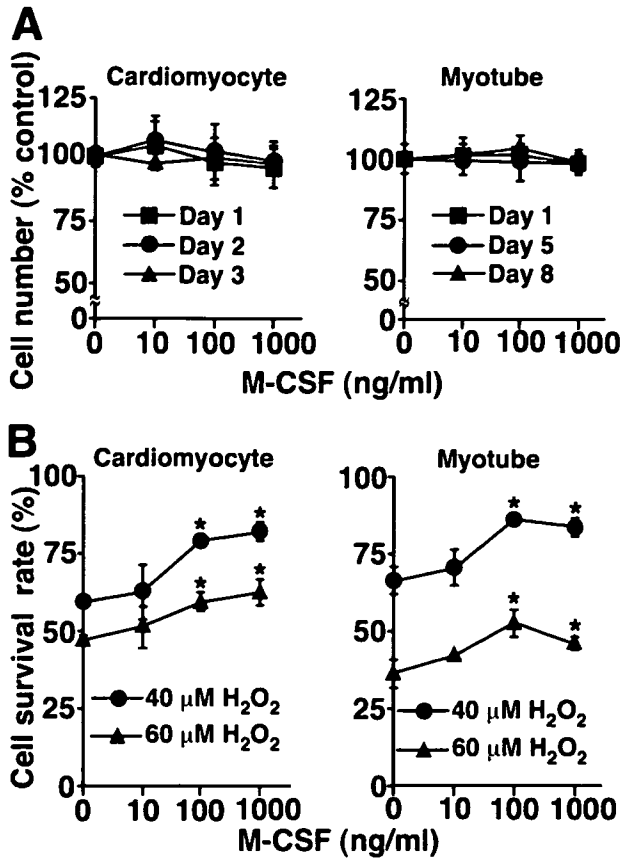


**Figure 4.** M-CSF protects differentiated H9c2 cells from $H_2O_2$-induced cell death. **A:** H9c2 cardiomyocytes were cultured with the indicated amount of M-CSF and ATRA for the indicated time periods, and the culture medium was changed daily. H9c2 myotubes were cultured with the indicated amount of M-CSF for the indicated time periods. WST assay determined the cell number. **B:** H9c2 cardiomyocytes or H9c2 myotubes were cultured with the indicated amount of M-CSF for 24 hours and then stimulated with $H_2O_2$ (40 or 60 μmol/L) for 8 hours. The culture medium of H9c2 cardiomyocytes was supplemented with ATRA. WST assay determined the cell viability. M-CSF (100 and 1000 ng/ml) significantly protected the cells from $H_2O_2$-induced cell death ($^*P < 0.03$). Similar results were obtained from three independent experiments.

cells.[11] Therefore, the cell survival effect of M-CSF on differentiated H9c2 cells from cytotoxic $H_2O_2$ exposure was examined. H9c2 cardiomyocytes were incubated with M-CSF and then exposed to $H_2O_2$. M-CSF significantly protected H9c2 cardiomyocytes from $H_2O_2$-induced cell death (Figure 4B). Similar results were obtained from H9c2 myotubes (Figure 4B).

### *M-CSF Activates ERK and Akt Signaling Pathways and Increases Bcl-xL Expression in Differentiated H9c2 Cells*

The cell signaling pathways of M-CSF in cardiomyocytes and H9c2 myotubes have not been investigated. To elucidate molecular mechanisms of the M-CSF-induced cell survival, differentiated H9c2 cells were treated with M-CSF and then activation of ERK, Akt, and Jak-STAT signaling pathways was investigated. Western blot analysis showed two forms of M-CSF-R in differentiated H9c2 cells (Figure 5, A and C).[30] In H9c2 cardiomyocytes, M-CSF induced ERK activation, as indicated by its protein phosphorylation, whereas the protein levels of the total ERK in cell lysates were not different (Figure 5A). M-CSF activated the Akt, but M-CSF did not activate Jak1, Stat1, or Stat3 (Figure 5A). ERK activation protects cardiomyocytes from cell death by up-regulating the anti-apoptotic protein Bcl-xL and inactivating the apoptotic protein Bad by its phosphorylation at Ser112.[31,32] Akt activation improves cardiomyocyte survival, but the main downstream signaling pathways of Akt for cardiomyocytes survival has not been clarified.[33] To clarify the target molecules of ERK in H9c2 cardiomyocytes, Bcl-xL expression was examined. Bcl-xL was detected in cells without M-CSF stimulation (Figure 5B). M-CSF up-regulated Bcl-xL expression, which peaked at 24 and 48 hours (Figure 5B). M-CSF did not phosphorylate Bad at Ser112 (Figure 5B). These results suggest M-CSF protected H9c2 cardiomyocytes by activating Akt and up-regulating Bcl-xL expression through ERK activation. In H9c2 myotubes, M-CSF activated ERK and Akt but did not activate Jak1 or Stat3

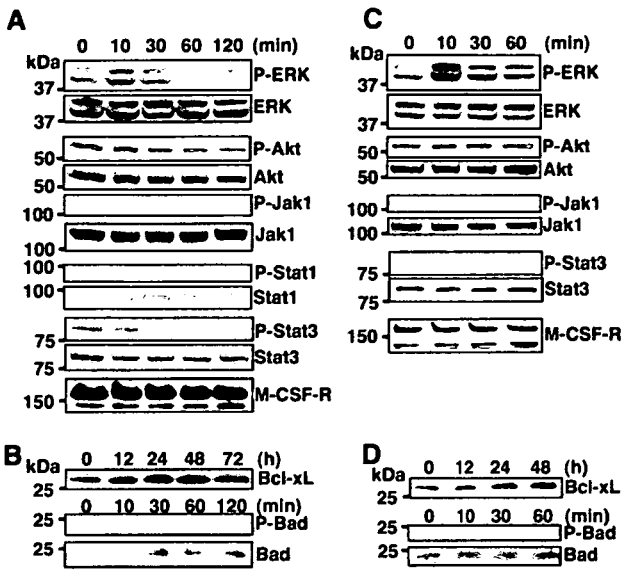


**Figure 5.** M-CSF activated ERK, Akt, and up-regulated Bcl-xL expression in differentiated H9c2 cells. H9c2 cardiomyocytes (**A** and **B**) or H9c2 myotubes (**C** and **D**) were stimulated with M-CSF (100 ng/ml) for the indicated time periods, and then the cell lysates were blotted with antibodies specific for the activated form of ERK (phospho-ERK), Akt (phospho-Akt), Jak1 (phospho-Jak1), Stat1 (phospho-Stat1), Stat3 (phospho-Stat3), or phosphorylated Bad (phospho-Bad). The membranes were reblotted with antibodies to total ERK, Akt, Jak1, Stat1, Stat3, or Bad, respectively. Expression of M-CSF-R or Bcl-xL was confirmed by blotting the membrane with specific antibodies. Similar results were obtained from three independent experiments.

(Figure 5C). M-CSF gradually up-regulated Bcl-xL expression until 48 hours (Figure 5D) but did not phosphorylate Bad at Ser112 (Figure 5D).

## *The Role of M-CSF-Induced Akt and ERK Activation in VEGF Production and Cell Survival in Differentiated H9c2 Cells*

M-CSF increases VEGF production through Akt activation in skeletal muscles. To determine the role of Akt activation in H9c2 cardiomyocytes VEGF production, H9c2 cardiomyocytes were treated with Akt-specific inhibitor LY294002, and the culture supernatant was assayed by ELISA. LY294002 and M-CSF treatment for 2 days significantly impaired VEGF production in H9c2 cardiomyocytes (Figure 6A). LY294002 and M-CSF treatment for 3 days further decreased VEGF production, and the VEGF level became less than the detection level (Figure 6A). To determine the role of ERK and Akt activation after M-CSF treatment in differentiated H9c2 cell survival, differentiated H9c2 cells were treated with LY294002 or the ERK-specific inhibitor PD98059. PD98059 inhibited ERK activation and LY294002 inhibited Akt activation in H9c2 cardiomyocytes (Figure 6B). Similar results were obtained from H9c2 myotubes (data not shown). PD98059 enhanced $H_2O_2$-induced cell death of H9c2 cardiomyocytes (Figure 6C). The protective effect of M-CSF was impaired by PD98059; however, M-CSF significantly protected H9c2 cardiomyocytes from cell death (Figure 6C). A similar result was obtained from LY294002 in H9c2 cardiomyocytes (Figure 6C). In H9c2 myotubes, PD 98059 enhanced $H_2O_2$-induced cell death, and PD98059

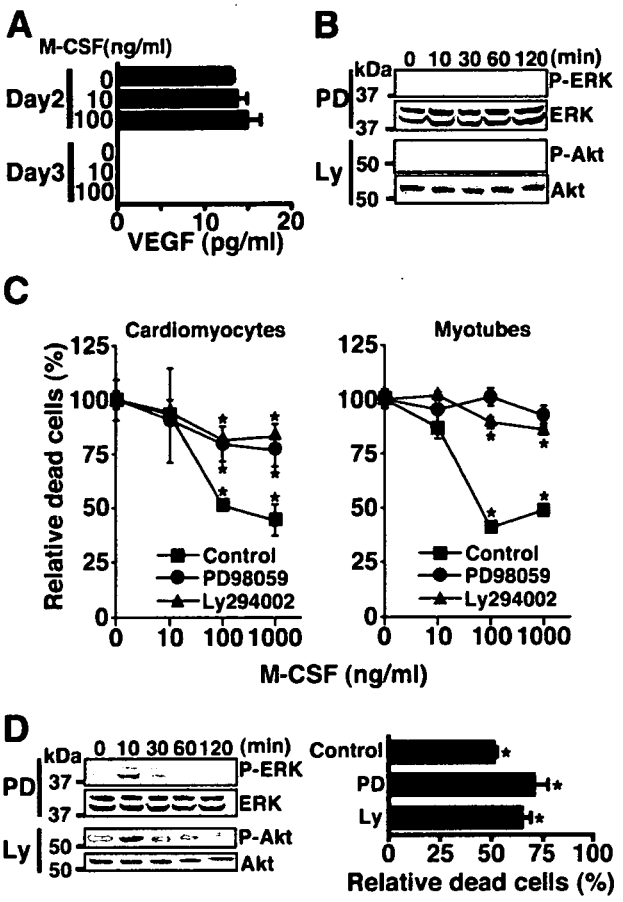


**Figure 6.** The role of M-CSF-induced Akt and ERK activation in VEGF production and cell protection in differentiated H9c2 cells. **A:** H9c2 cardiomyocytes were cultured with M-CSF and 10 μmol/L LY294002 for the indicated time periods. The culture medium was changed daily and ELISA determined the VEGF level. **B:** H9c2 cardiomyocytes were incubated with 30 μmol/L PD98059 (PD) or 10 μmol/L LY294002 (Ly) for 30 minutes, then stimulated with M-CSF (100 ng/ml) and inhibitors, and analyzed as described in Figure 5. **C:** Differentiated H9c2 cells were stimulated with indicated amount of M-CSF with PD98059 (30 μmol/L) or LY294002 (10 μmol/L) for 24 hours. Then the cells were stimulated with $H_2O_2$ (40 μmol/L) for 8 hours, and WST assay determined the dead cells. M-CSF (0 ng/ml) in each group is considered as 100%, and relative cell death rates in each group are shown. $^*P < 0.03$ compared with 0 ng/ml M-CSF in each group. Similar results were obtained from three independent experiments. **D:** H9c2 cardiomyocytes were incubated with reduced concentrations of PD98059 (6 μmol/L) or LY294002 (2 μmol/L). Left: H9c2 cardiomyocytes were treated with PD98059 or LY294002 for 30 minutes, stimulated with M-CSF (100 ng/ml) and inhibitors, and then analyzed as described in Figure 5. Right: H9c2 cardiomyocytes were treated with PD98059, LY294002, or without inhibitors (control) with (100 ng/ml) or without (0 ng/ml) M-CSF for 24 hours. Then the cells were stimulated with $H_2O_2$ (40 μmol/L) for 8 hours, and dead cells were assessed by WST assay. In each inhibitor group, dead cells at 0 ng/ml M-CSF are considered as 100%, and relative cell death rates at 100 to 0 ng/ml M-CSF in each inhibitor group are shown. $^*P < 0.02$ compared with 0 ng/ml M-CSF in each group.

abolished the protective effect of M-CSF (Figure 6C). LY294002 enhanced $H_2O_2$-induced cell death in H9c2 myotubes; however, M-CSF significantly protected H9c2 myotubes from cell death (Figure 6C). Moreover, a dose-response experiment of PD98059 or LY294002 was performed to observe ERK or Akt phosphorylation and cellular survival of H9c2 cardiomyocytes (Figure 6D). Similar results were obtained from H9c2 myotubes (data not shown). VEGF protected myogenic cells from cell death.[34] To confirm whether the cell survival effect of M-CSF de-

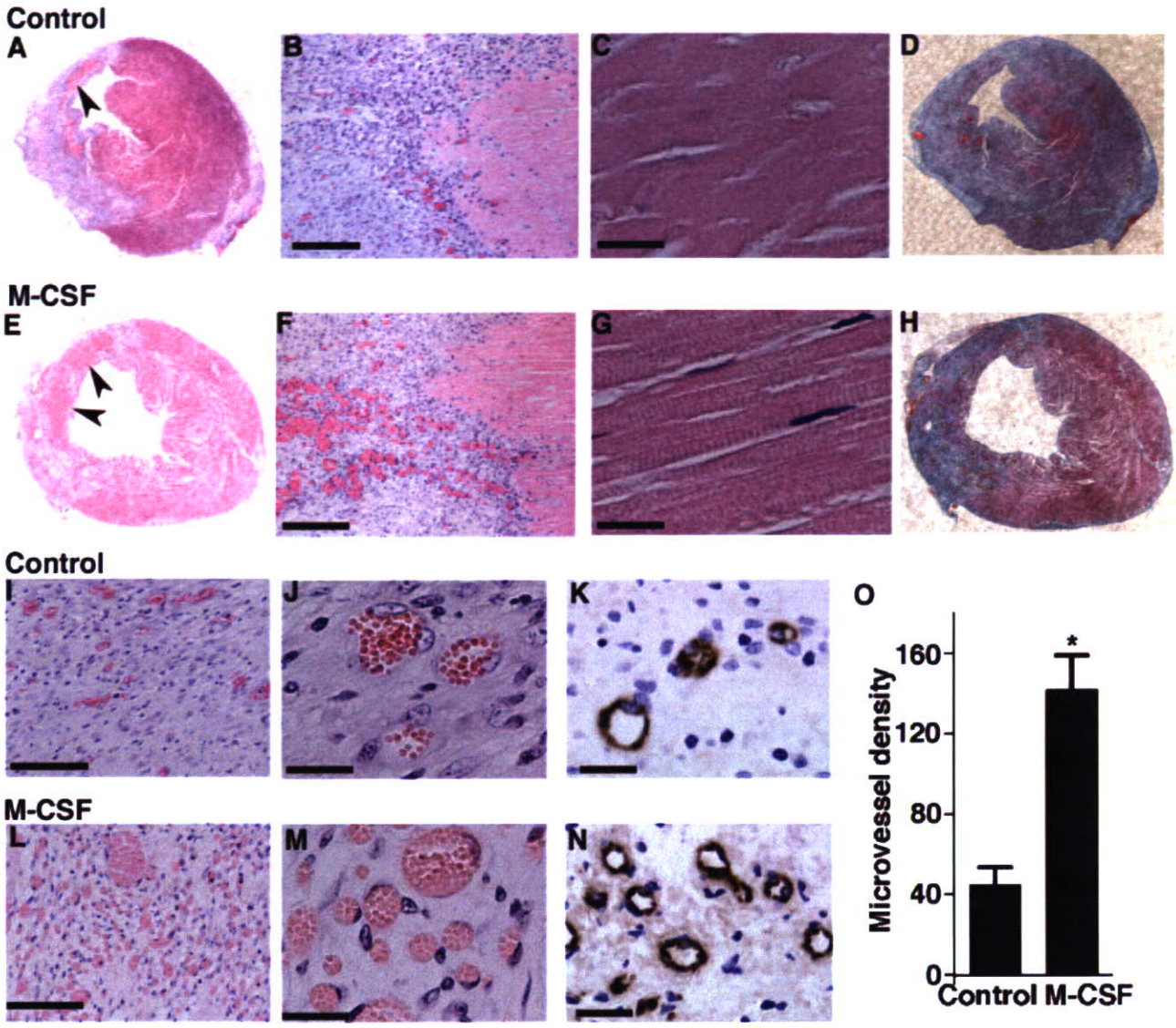


**Figure 7.** M-CSF promotes angiogenesis in goat heart after myocardial infarction. The goat left anterior descending coronary artery was permanently ligated, and the goats were sacrificed on day 14. M-CSF indicates goats intravenously injected with M-CSF shortly after the coronary artery ligation daily until day 13. Controls were injected with saline. Paraffin sections were stained with H&E (**A–C**, **E–G**, **I**, **J**, **L**, and **M**), Masson's elastic stain (**D** and **H**), and anti-factor VIII-related antigen antibody (**K** and **N**). **A** and **E:** Left anterior descending coronary artery ligation induced myocardial infarction. **Arrowheads** indicate cardiomyocytes in ischemic lesions. (**B**, **C**, **F**, and **G**) Microscopic observations indicated the cardiomyocytes in the ischemic lesions were dead. **D** and **H:** The green staining indicates fibrosis or scars in hearts. **I**, **J**, **L**, and **M:** The microvessels in ischemic lesions. **K** and **N:** The microvessels in ischemic lesions were immunohistochemically stained with anti-factor VIII-related antigen antibody. **O:** M-CSF significantly increased microvessel density in ischemic lesions ($^*P < 0.01$, $n = 3$ per group). The images represent one of three goats in each group. Scale bars: 200 μm (**B** and **F**); 20 μm (**C**, **G**, **J**, **K**, **M**, and **N**); 100 μm (**I** and **L**).

pends on VEGF, H9c2 cardiomyocytes and myotubes were cultured with an anti-VEGF antibody and M-CSF. Incubation with anti-VEGF antibody did not impair the cell protective effect of M-CSF from $H_2O_2$ stimulation suggesting that the effect of M-CSF was not VEGF-dependent (data not shown).

### *M-CSF Promotes Angiogenesis in Goat Ischemic Heart after Permanent Coronary Artery Ligation*

M-CSF treatment elevated systemic VEGF level in mice from a nondetectable level to potentially therapeutic levels.[14,15] The cell protective and angiogenic effects of M-CSF *in vivo* were examined using goats as a large animal model for myocardial infarction. Large animal models are necessary for evaluating growth factor-induced therapeutic angiogenesis,[3] and we have used goats for developing artificial heart devices.[27] We induced myocardial infarction by permanent left anterior descending coronary artery ligation. The coronary artery ligation resulted in LV infarction (Figure 7, A, D, E, and H). Macroscopically, M-CSF seemed to promote cardiomyocyte cell survival in ischemic lesions in comparison to the controls (Figure 7, A and E; arrowheads). Microscopy indicated that cardiomyocytes in ischemic lesions were dead cells in the controls (Figure 7, B and C). At low magnification, M-CSF seemed to protect cardiomyocytes from cell death in ischemic lesions (Figure 7F). However,

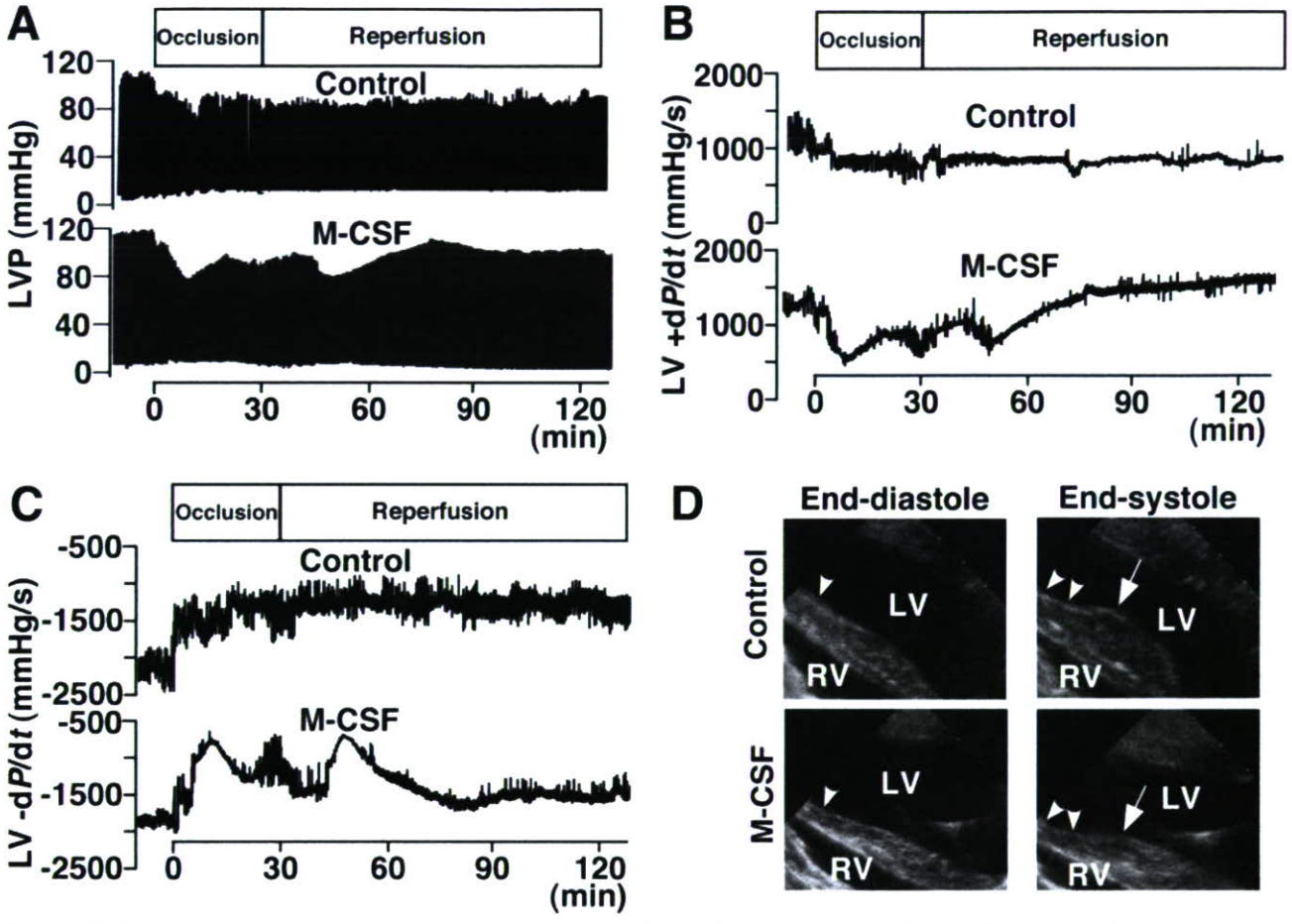


**Figure 8.** M-CSF pretreatment improved cardiac function after ischemic injury. M-CSF indicates goats intravenously injected with M-CSF daily for 3 days, whereas the control indicates goats injected with saline. The goat left anterior descending coronary artery was occluded for 30 minutes and then reperfused. **A–C:** Hemodynamic parameters before and during 30 minutes of left anterior descending coronary artery occlusion followed by 90 minutes of reperfusion are shown. Representative LVP records (**A**), representative positive dP/dt (**B**), and representative negative dP/dt (**C**) of control and M-CSF-treated goats. LVEDP, positive and negative dP/dt recovered in M-CSF-treated goats after reperfusion. **D: Arrowheads** indicate infarct areas. Compare **arrows**, which indicate wall contraction of nonischemic area at end systole, to **arrowheads**. In the infarct area, echocardiography shows dyskinetic wall movement in controls, whereas akinetic wall movement is shown in M-CSF-treated goats. Data are representative of three goats in each group.

at high magnification, most of the cardiomyocytes were dead (Figure 7G). Microvessels were observed in the ischemic lesions of control goats (Figure 7, I and J), and M-CSF treatment increased the number of microvessels (Figure 7, L and M). To confirm the microvessel density, we immunohistochemically stained goat hearts with anti-factor VIII-related antigen antibody (Figure 8, K and N).[23,24] M-CSF significantly increased microvessel density in ischemic lesions by 226% (Figure 7O). These results suggest that M-CSF promoted angiogenesis and induced collateral blood vessels in the ischemic heart. The infarct area quantification showed no significant difference between control and M-CSF-treated goats (controls, 30.4 ± 5.2%; M-CSF, 24.3 ± 2.1%). The residual presence of nuclei and cross striations in dead cardiomyocytes in ischemic lesions by M-CSF treatment (Figure 7G) suggests that the cardiomyocytes survived longer than control cardiomyocytes (Figure 7, C and G), but M-CSF-induced new vessels could not reach cardiomyocytes in ischemic lesions before their death.

### *M-CSF Pretreatment Improved Cardiac Function after Ischemic Injury Induced by Coronary Artery Occlusion-Reperfusion*

Erythropoietin treatment did not change the infarct size, but it improved cardiac function in the rat coronary artery occlusion-reperfusion model.[5] Pretreatment with stem cell factor and G-CSF improved cardiac function after myocardial infarction.[7] To confirm further the effects of M-CSF in myocardial infarction, goats were pretreated with M-CSF for 3 days, and then myocardial infarction was induced by 30-minute left anterior descending coronary artery occlusion followed by reperfusion.[5,35] Cardiac function was assessed by measuring hemodynamic parameters using catheterization analysis and examining echocardiography. Echocardiographic examination showed no significant differences in basal findings in cardiac function in both groups. Catheterization analysis showed the LV pressure (LVP) records of control and M-CSF-treated goats (Figure 8A). LV end diastolic pressure

(LVEDP), which can influence overall cardiac function,[4] increased after the left anterior descending coronary artery occlusion in both groups. In controls, the LVEDP did not recover after reperfusion, but in M-CSF-treated goats, the LVEDP gradually recovered after reperfusion (Figure 8A), and at 90 minutes after the reperfusion, the LVEDP of M-CSF treated goats was significantly better than that of control goats (controls, 10.62 ± 0.98 mmHg; M-CSF, 7.61 ± 0.83 mmHg; $P < 0.02$). Positive and negative dP/dt are measures of overall cardiac contractility and relaxation, respectively.[4] Positive dP/dt decreased after the left anterior descending coronary artery occlusion both in control and M-CSF-treated goats (Figure 8B). After reperfusion, positive dP/dt did not recover in control goats (Figure 8B). In M-CSF treated goats, positive dP/dt gradually recovered after reperfusion and finally reached similar dP/dt levels before the occlusion (Figure 8B). At 90 minutes after the reperfusion, the positive dP/dt of M-CSF-treated goats was significantly better than that of control goats (controls, 886 ± 103 mmHg; M-CSF, 1506 ± 125 mmHg; $P < 0.01$). Moreover, recovery of negative dP/dt after left anterior descending coronary artery occlusion-reperfusion was observed only in M-CSF-treated goats (Figure 8C). At 90 minutes after the reperfusion, the negative dP/dt of M-CSF-treated goats was significantly better than that of control goats (controls, −1342 ± 92 mmHg; M-CSF, −1570 ± 108 mmHg; $P < 0.05$). Echocardiographic examination showed a paradoxical LV wall movement area indicated as a dyskinetic area after left anterior descending coronary artery occlusion in control goats (Figure 8D). In M-CSF-treated goats, echocardiography showed a LV wall movement arrest area indicated as an akinetic area after left anterior descending coronary artery occlusion, and a dyskinetic area could not be found (Figure 8D). In control hearts, the nonischemic wall contractions at end systole were enhanced. This suggested substitutive wall movement for the dyskinetic area to keep cardiac output (Figure 8D). These echocardiographic findings suggest improvement of LV wall movement in M-CSF-treated goats during left anterior descending coronary artery occlusion-reperfusion. The LV ejection fraction (LVEF) was evaluated by echocardiography, but LVEF did not significantly change between before and after the occlusion; therefore, LVEF between controls and M-CSF-treated ones were not compared. Recovery of LVEDP, positive and negative *dP/dt* after reperfusion, and improvement of LV wall movement during the left anterior descending coronary artery occlusion-reperfusion suggest M-CSF pretreatment improved cardiac function after ischemic injury.

## *Discussion*

In this study, M-CSF increased VEGF production in hearts both *in vivo* and *in vitro*. *In vitro*, M-CSF increased VEGF production through Akt activation. Moreover, M-CSF directly protected cardiomyocytes from cell death by activating Akt and ERK resulting in up-regulation of the downstream anti-apoptotic protein Bcl-xL. M-CSF-R expression in the heart was shown both *in vivo* and *in vitro*, and these results suggest that the expression is functional. Similar cell-protective effects of M-CSF on H9c2 myotubes were shown. *In vivo*, M-CSF treatment after the onset of myocardial infarction promoted angiogenesis in the ischemic heart, suggesting development of collateral blood vessels. Furthermore, M-CSF pretreatment in the goat myocardial infarction model improves cardiac function, as indicated by improvement of LVEDP, positive and negative dP/dt, and LV wall movements.

Recent studies indicate intramyocardial transfer of plasmid or adenoviral DNA-encoding human VEGF has favorable effects in myocardial infarction animal models and in patients with coronary artery diseases.[1,2,36] Similar to these VEGF transfer strategies, M-CSF directly up-regulated VEGF production in cardiomyocytes. In addition, M-CSF significantly induced an increase in plasma VEGF in mice to therapeutic levels that induced therapeutic angiogenesis.[14,35] Therapeutic plasmid gene delivery to a target organ is difficult and often temporary. However, M-CSF treatment was easily achieved by peripheral intravenous or intramuscular injection. These data indicate a therapeutic potential of M-CSF in ischemic heart diseases. Basic fibroblast growth factor and hepatocyte growth factor have also been applied to therapeutic angiogenesis.[37] We treated mice with M-CSF and examined basic fibroblast growth factor and hepatocyte growth factor mRNA levels by quantitative RT-PCR. M-CSF did not increase basic fibroblast growth factor or hepatocyte growth factor mRNA levels in the heart (data not shown). We also examined plasma G-CSF level after M-CSF treatment in mice by ELISA. M-CSF did not increase plasma G-CSF level. However, there is still a possibility that M-CSF induces other factors that are responsible for the effects shown in this article.

Very recently, M-CSF was reported to accelerate infarct repair and attenuate LV dysfunction in rats.[35] However, these authors did not investigate VEGF induction or the cardioprotective effects of M-CSF and did not use a large animal model. In the present study, in the M-CSF-treated group, we observed an increase in microvessel density, increased presence of dead cardiomyocytes, and decreased presence of granuloma in ischemic lesions. The increased presence of dead cardiomyocytes in ischemic lesions and improvement of cardiac function after ischemia in M-CSF-treated goats suggest a longer survival of cardiomyocytes in M-CSF-treated goats than in the controls. This finding and the decreased presence of granuloma suggest that M-CSF reduced the progression rate of ischemic injury in ischemic hearts *in vivo*.

In human monocytes, LY294002 suppressed M-CSF-induced ERK activation.[38] This mechanism was explained as M-CSF stimulation-induced reactive oxygen species, which activated ERK. The addition of Akt inhibitor prevented reactive oxygen species production and thus suppressed ERK activation in M-CSF-stimulated monocytes.[38] In murine myeloid cell line FDC-P1, LY294002 suppressed M-CSF-induced ERK activation, but it was not significant.[39] In H9c2 cardiomyocytes, LY294002 seemed to impair ERK activation in part. To suggest the involvement of Akt in M-CSF-induced ERK

activation in cardiomyocytes, we may have to use other Akt-inhibiting methods, as this time we could not reach a clear conclusion. For VEGF production, PD98059 treatment for 1 day did not affect M-CSF-induced VEGF production in differentiated H9c2 cells, whereas LY294002 treatment impaired M-CSF-induced VEGF production, suggesting M-CSF-induced VEGF production in differentiated H9c2 cells were Akt-dependent. This is the first report that suggested the presence of signal transduction pathways in cardiomyocytes in response to M-CSF. Further experiments are required for pursuing the M-CSF-induced intracellular signaling pathways in cardiomyocytes or in myotubes.

Goat hearts have a left coronary artery-dominant blood supply.[40] The goat coronary artery anatomy was remarkably regular, and coronary artery collaterals could not be demonstrated,[40] indicating frailty after heart ischemic injury. For the left anterior descending coronary artery occlusion-reperfusion model, the goat left anterior descending coronary artery was ligated at a point ~40% from the beginning of the left coronary artery to the apex, but LVEF decrease could not be detected by echocardiography. Occlusion of a more proximal site of goat left anterior descending coronary artery has been reported to be invariably fatal,[40] and our preliminary experiments with a more proximal left anterior descending coronary artery ligation supported this finding. Therefore, using goats, LVEF after myocardial infarction could not be evaluated. We were not able to assess plasma VEGF and the involvement of bone marrow-derived cells in the goat model because the appropriate reagents are not commercially available. We could not find a staining method specific for cardiomyocyte viability in goat hearts. Infarct area quantification suggested a trend that M-CSF might decrease infarct area. However, infarct area quantification showed no significant difference in control and M-CSF-treated goat hearts. Further investigation is required to clarify the roles and mechanisms of M-CSF in ischemic diseases using other species and other M-CSF treatment protocols.

The cell-protective and VEGF-inducing effects of M-CSF both in cardiomyocytes and myotubes were shown, and the effects were confirmed by improvement of cardiac function and activated angiogenesis in goat ischemic hearts. M-CSF is already in use clinically, and data from patients such as side effects are accumulating. Moreover, M-CSF administration is easily performed with minimal invasiveness in human patients. In this study, we showed the potential benefits of M-CSF treatment and its new mechanisms in ischemic heart diseases.

## Acknowledgments

We thank Peter Baluk, Hiroya Hashizume, Hiroshi Kubo, and Katsutoshi Nakayama for helpful comments on the manuscript; and Amy Ni and Shannon Freeman for correcting the manuscript.

## References

1. Yoon YS, Johnson IA, Park JS, Diaz L, Losordo DW: Therapeutic myocardial angiogenesis with vascular endothelial growth factors. Mol Cell Biochem 2004, 264:63–74
2. Kastrup J, Jorgensen E, Ruck A, Tagil K, Glogar D, Ruzyllo W, Botker HE, Dudek D, Drvota V, Hesse B, Thuesen L, Blomberg P, Gyongyosi M, Sylven C: Direct intramyocardial plasmid vascular endothelial growth factor-A165 gene therapy in patients with stable severe angina pectoris A randomized double-blind placebo-controlled study: the Euroinject One trial. J Am Coll Cardiol 2005, 45:982–988
3. Markkanen JE, Rissanen TT, Kivela A, Yla-Herttuala S: Growth factor-induced therapeutic angiogenesis and arteriogenesis in the heart-gene therapy. Cardiovasc Res 2005, 65:656–664
4. Parsa CJ, Matsumoto A, Kim J, Riel RU, Pascal LS, Walton GB, Thompson RB, Petrofski JA, Annex BH, Stamler JS, Koch WJ: A novel protective effect of erythropoietin in the infarcted heart. J Clin Invest 2003, 112:999–1007
5. Calvillo L, Latini R, Kajstura J, Leri A, Anversa P, Ghezzi P, Salio M, Cerami A, Brines M: Recombinant human erythropoietin protects the myocardium from ischemia-reperfusion injury and promotes beneficial remodeling. Proc Natl Acad Sci USA 2003, 100:4802–4806
6. Harada M, Qin Y, Takano H, Minamino T, Zou Y, Toko H, Ohtsuka M, Matsuura K, Sano M, Nishi J, Iwanaga K, Akazawa H, Kunieda T, Zhu W, Hasegawa H, Kunisada K, Nagai T, Nakaya H, Yamauchi-Takihara K, Komuro I: G-CSF prevents cardiac remodeling after myocardial infarction by activating the Jak-Stat pathway in cardiomyocytes. Nat Med 2005, 11:305–311
7. Orlic D, Kajstura J, Chimenti S, Limana F, Jakoniuk I, Quaini F, Nadal-Ginard B, Bodine DM, Leri A, Anversa P: Mobilized bone marrow cells repair the infarcted heart, improving function and survival. Proc Natl Acad Sci USA 2001, 98:10344–10349
8. Miki T, Miura T, Nishino Y, Yano T, Sakamoto J, Nakamura Y, Ichikawa Y, Ikeda Y, Kobayashi H, Ura N, Shimamoto K: Granulocyte colony stimulating factor/macrophage colony stimulating factor improves postinfarct ventricular function by suppression of border zone remodelling in rats. Clin Exp Pharmacol Physiol 2004, 31:873–882
9. Ohno R, Miyawaki S, Hatake K, Kuriyama K, Saito K, Kanamaru A, Kobayashi T, Kodera Y, Nishikawa K, Matsuda S, Yamada O, Omoto E, Takeyama H, Tsukuda K, Asou N, Tanimoto M, Shiozaki H, Tomonaga M, Masaoka T, Miura Y, Takaku F, Ohashi Y, Motoyoshi K: Human urinary macrophage colony-stimulating factor reduces the incidence and duration of febrile neutropenia and shortens the period required to finish three courses of intensive consolidation therapy in acute myeloid leukemia: a double-blind controlled study. J Clin Oncol 1997, 15:2954–2965
10. Kawakami Y, Nagai N, Ohama K, Zeki K, Yoshida Y, Kuroda E, Yamashita U: Macrophage-colony stimulating factor inhibits the growth of human ovarian cancer cells in vitro. Eur J Cancer 2000, 36:1991–1997
11. Stanley ER, Berg KL, Einstein DB, Lee PS, Pixley FJ, Wang Y, Yeung YG: Biology and action of colony-stimulating factor-1. Mol Reprod Dev 1997, 46:4–10
12. Giordano FJ, Gerber HP, Williams SP, VanBruggen N, Bunting S, Ruiz-Lozano P, Gu Y, Nath AK, Huang Y, Hickey R, Dalton N, Peterson KL, Ross Jr J, Chien KR, Ferrara N: A cardiac myocyte vascular endothelial growth factor paracrine pathway is required to maintain cardiac function. Proc Natl Acad Sci USA 2001, 98:5780–5785
13. Maharaj AS, Saint-Geniez M, Maldonado AE, D'Amore PA: Vascular endothelial growth factor localization in the adult. Am J Pathol 2006, 168:639–648
14. Okazaki T, Ebihara S, Takahashi H, Asada M, Kanda A, Sasaki H: Macrophage colony-stimulating factor induces vascular endothelial growth factor production in skeletal muscle and promotes tumor angiogenesis. J Immunol 2005, 174:7531–7538
15. Kalka C, Masuda H, Takahashi T, Gordon R, Tepper O, Gravereaux E, Pieczek A, Iwaguro H, Hayashi SI, Isner JM, Asahara T: Vascular endothelial growth factor$_{165}$ gene transfer augments circulating endothelial progenitor cells in human subjects. Circ Res 2000, 86:1198–1202
16. Kallies A, Rosenbauer F, Scheller M, Knobeloch KP, Horak I: Accumulation of c-Cbl and rapid termination of colony-stimulating factor 1 receptor signaling in interferon consensus sequence bind-

ing protein-deficient bone marrow-derived macrophages. Blood 2002, 99:3213–3219
17. Novak U, Harpur AG, Paradiso L, Kanagasundaram V, Jaworowski A, Wilks AF, Hamilton JA: Colony-stimulating factor 1-induced STAT1 and STAT3 activation is accompanied by phosphorylation of Tyk2 in macrophages and Tyk2 and JAK1 in fibroblasts. Blood 1995, 86:2948–2956
18. Kelley TW, Graham MM, Doseff AI, Pomerantz RW, Lau SM, Ostrowski MC, Franke TF, Marsh CB: Macrophage colony-stimulating factor promotes cell survival through Akt/protein kinase B. J Biol Chem 1999, 274:26393–26398
19. Ménard C, Pupier S, Mornet D, Kitzmann M, Nargeot J, Lory P: Modulation of L-type calcium channel expression during retinoic acid-induced differentiation of H9C2 cardiac cells. J Biol Chem 1999, 274:29063–29070
20. van den Eijnde SM, van den Hoff MJ, Reutelingsperger CP, van Heerde WL, Henfling ME, Vermeij-Keers C, Schutte B, Borgers M, Ramaekers FC: Transient expression of phosphatidylserine at cell-cell contact areas is required for myotube formation. J Cell Sci 2001, 114:3631–3642
21. Kang YJ, Zhou ZX, Wang GW, Buridi A, Klein JB: Suppression by metallothionein of doxorubicin-induced cardiomyocyte apoptosis through inhibition of p38 mitogen-activated protein kinases. J Biol Chem 2000, 275:13690–13698
22. Okazaki T, Sakon S, Sasazuki T, Sakurai H, Doi T, Yagita H, Okumura K, Nakano H: Phosphorylation of serine 276 is essential for p65 NF-κB subunit-dependent cellular responses. Biochem Biophys Res Commun 2003, 300:807–812
23. Seno H, Oshima M, Ishikawa TO, Oshima H, Takaku K, Chiba T, Narumiya S, Taketo MM: Cyclooxygenase 2- and prostaglandin $E_2$ receptor $EP_2$-dependent angiogenesis in $Apc^{\Delta 716}$ mouse intestinal polyps. Cancer Res 2002, 62:506–511
24. Bildfell RJ, Valentine BA, Whitney KM: Cutaneous vasoproliferative lesions in goats. Vet Pathol 2002, 39:273–277
25. Ebihara S, Guibinga GH, Gilbert R, Nalbantoglu J, Massie B, Karpati G, Petrof BJ: Differential effects of dystrophin and utrophin gene transfer in immunocompetent muscular dystrophy (mdx) mice. Physiol Genomics 2000, 3:133–144
26. Sakon S, Xue X, Takekawa M, Sasazuki T, Okazaki T, Kojima Y, Piao JH, Yagita H, Okumura K, Doi T, Nakano H: NF-κB inhibits TNF-induced accumulation of ROS that mediate prolonged MAPK activation and necrotic cell death. EMBO J 2003, 22:3898–3909
27. Wang Q, Yambe T, Shiraishi Y, Duan X, Nitta S, Tabayashi K, Umezu M: An artificial myocardium assist system: electrohydraulic ventricular actuation improves myocardial tissue perfusion in goats. Artif Organs 2004, 28:853–857
28. Kim WG, Cho SR, Sung SH, Park HJ: A chronic heart failure model by coronary artery ligation in the goat. Int J Artif Organs 2003, 26:929–934
29. Eubank TD, Galloway M, Montague CM, Waldman WJ, Marsh CB: M-CSF induces vascular endothelial growth factor production and angiogenic activity from human monocytes. J Immunol 2003, 171:2637–2643
30. Ide H, Seligson DB, Memarzadeh S, Xin L, Horvath S, Dubey P, Flick MB, Kacinski BM, Palotie A, Witte ON: Expression of colony-stimulating factor 1 receptor during prostate development and prostate cancer progression. Proc Natl Acad Sci USA 2002, 99:14404–14409
31. Baines CP, Molkentin JD: STRESS signaling pathways that modulate cardiac myocyte apoptosis. J Mol Cell Cardiol 2005, 38:47–62
32. Valks DM, Cook SA, Pham FH, Morrison PR, Clerk A, Sugden PH: Phenylephrine promotes phosphorylation of Bad in cardiac myocytes through the extracellular signal-regulated kinases 1/2 and protein kinase A. J Mol Cell Cardiol 2002, 34:749–763
33. Matsui T, Rosenzweig A: Convergent signal transduction pathways controlling cardiomyocyte survival and function: the role of PI 3-kinase and Akt. J Mol Cell Cardiol 2005, 38:63–71
34. Arsic N, Zacchigna S, Zentilin L, Ramirez-Correa G, Pattarini L, Salvi A, Sinagra G, Giacca M: Vascular endothelial growth factor stimulates skeletal muscle regeneration in vivo. Mol Ther 2004, 10:844–854
35. Yano T, Miura T, Whittaker P, Miki T, Sakamoto J, Nakamura Y, Ichikawa Y, Ikeda Y, Kobayashi H, Ohori K, Shimamoto K: Macrophage colony-stimulating factor treatment after myocardial infarction attenuates left ventricular dysfunction by accelerating infarct repair. J Am Coll Cardiol 2006, 47:626–634
36. Rutanen J, Rissanen TT, Markkanen JE, Gruchala M, Silvennoinen P, Kivela A, Hedman A, Hedman M, Heikura T, Orden MR, Stacker SA, Achen MG, Hartikainen J, Yla-Herttuala S: Adenoviral catheter-mediated intramyocardial gene transfer using the mature form of vascular endothelial growth factor-D induces transmural angiogenesis in porcine heart. Circulation 2004, 109:1029–1035
37. Azuma J, Taniyama Y, Takeya Y, Iekushi K, Aoki M, Dosaka N, Matsumoto K, Nakamura T, Ogihara T, Morishita R: Angiogenic and antifibrotic actions of hepatocyte growth factor improve cardiac dysfunction in porcine ischemic cardiomyopathy. Gene Ther 2006, 13:1206–1213
38. Bhatt NY, Kelley TW, Khramtsov VV, Wang Y, Lam GK, Clanton TL, Marsh CB: Macrophage-colony-stimulating factor-induced activation of extracellular-regulated kinase involves phosphatidylinositol 3-kinase and reactive oxygen species in human monocytes. J Immunol 2002, 169:6427–6434
39. Gobert Gosse S, Bourgin C, Liu WQ, Garbay C, Mouchiroud G: M-CSF stimulated differentiation requires persistent MEK activity and MAPK phosphorylation independent of Grb2-Sos association and phosphatidylinositol 3-kinase activity. Cell Signal 2005, 17:1352–1362
40. Lipovetsky G, Fenoglio JJ, Gieger M, Srinivasan MR, Dobelle WH: Coronary artery anatomy of the goat. Artif Organs 1983, 7:238–245

ARTICLE IN PRESS

Available online at www.sciencedirect.com

ScienceDirect

Ultrasonics xxx (2007) xxx–xxx

Ultrasonics

www.elsevier.com/locate/ultras

# Fractal dimension of 40 MHz intravascular ultrasound radio frequency signals

E. Santos Filho [a,*], Y. Saijo [a], A. Tanaka [b], T. Yambe [a], M. Yoshizawa [c]

[a] *Department of Medical Engineering and Cardiology, Institute of Development, Aging, and Cancer, Tohoku University, 4-1 Seiryomachi, Aoba-ku, Sendai 980-8575, Japan*

[b] *Faculty of Symbiotic Systems Science, Fukushima University, Japan*

[c] *Information Synergy Center, Tohoku University, Japan*

Received 18 April 2007; received in revised form 24 August 2007; accepted 24 August 2007

**Abstract**

*Objective:* Fully automatic tissue characterization in intravascular ultrasound systems is still a challenge for the researchers. The present work aims to evaluate the feasibility of using the Higuchi fractal dimension of intravascular ultrasound radio frequency signals as a feature for tissue characterization.

*Methods:* Fractal dimension images are generated based on the radio frequency signals obtained using mechanically rotating 40 MHz intravascular ultrasound catheter (Atlantis SR Plus, Boston Scientific, USA) and compared with the corresponding correlation images.

*Conclusion:* An inverse relation between the fractal dimension images and the correlation images was revealed indicating that the hard or slow moving tissues in the correlation image usually have low fractal dimension and vice-versa. Thus, the present study suggests that fractal dimension images may be used as a feature for intravascular ultrasound tissue characterization and present better resolution then the correlation images.



*PACS:* 87.62; 87.59.M; 47.53.+n

*Keywords:* Intravascular ultrasound; Tissue characterization; Fractal dimension; Radio frequency signal; Coronary artery

## 1. Introduction

Intravascular ultrasound (IVUS) has been clinically applied since early 1990s. The tomographic orientation of ultrasound enables visualization of the entire circumference of the vessel wall and provide information about tissues beneath the luminal border. However, visual analysis of IVUS images by experts is usually accompanied by limitations associated with interpersonal variations, errors due to fatigue, environmental distractions, etc. Computer-aided tissue characterization of IVUS images has a potential to add objective strength to the interpretation of the expert becoming an important tool for coronary diseases diagnosis. Analysis of IVUS radio frequency (RF) signal has potential to provide powerful features for tissue characterization because it is the original source of information from the backscattered ultrasound beam.

Nair et al. [1] successfully used spectral analysis of backscattered IVUS RF signals to classify plaque composition by constructing classification trees. However, for test data, in spite of presenting accuracy of 100% for calcified-necrosis, the accuracies for fibrolipid and collagen were 83% and 69%, respectively, showing that improvements and new signal processing techniques are still necessary for a full tissue characterization in IVUS imaging.

Signal processing based on estimating fractal dimension in a time series has been successfully applied in a number of

* Corresponding author. Tel.: +81 22 717 8517; fax: +81 22 717 8518.
*E-mail address:* esmeraldo@ieee.org (E.S. Filho).

0041-624X/$ - see front matter © 2007 Elsevier B.V. All rights reserved.
doi:10.1016/j.ultras.2007.08.006

**Please cite this article in press as: E.S. Filho et al., Fractal dimension of 40 MHz intravascular ultrasound radio ..., Ultrasonics (2007), doi:10.1016/j.ultras.2007.08.006**

medical applications due to its capability of expressing signal irregularity [1–5].

Alacam et al. [6] showed that the features obtained by statistical modeling of RF echo can be used as decision criterion for tissue characterization in breast cancer diagnosis. They proposed the fractional differencing auto regressive moving average (FARMA) model which captures the fractal and long term correlated nature of the backscattered speckle texture. Using a linear classifier their method presented an area of 0.87 under the receiver operating characteristic (ROC) curve.

Moradi et al. [7] have presented an innovative approach for detection of prostate cancer based on the fractal analysis of RF ultrasound echo signals. They used Higuchi's [8] method to calculate the fractal dimension over a region of interest (ROI) and used it as feature to detect the prostate cancer through a Bayesian classifier [9]. Their algorithm presented accuracy of 86% indicating the feasibility of their approach.

Saijo et al. [10,11], have developed a method for tissue characterization based on two-dimensional correlation between two consecutive frames of an IVUS sequence. This technique was shown capable of distinguishing regions of fast moving fluid like blood or surrounding tissue from region of slow moving or stable like the vessel wall.

In this work, we investigate the feasibility of using the Higuchi's fractal dimension as a feature for tissue characterization in IVUS through comparison with correlation images.

## 2. Materials and methods

IVUS data were acquired with an IVUS console Clear View Ultra (Boston Scientific Inc., Natick-MA, USA) and 40 MHz mechanically rotating IVUS catheter Atlantis SR Plus (Boston Scientific Inc., Natick-MA, USA) and the pulse repetition rate was 7680 Hz. RF data were digitized and stored in a personal computer (PC) (Dell 8250, Pentium 4, 2.4 GHz, 1.50 GB RAM, Dell Inc., Round Rock, TX, USA) using an A/D board GAGE Compuscope 8500 (500 Msamples/s, with 8 bits of resolution, Gage Applied Inc., Montreal, Quebec, Canada) for off-line analysis. The algorithms were developed using MATLAB (The Mathworks Inc., Natick, MA, USA). A single frame of the IVUS system consisted of 256 lines so that 7680 pulses made 30 frames per second (f/s). RF signal data were acquired in vivo from 14 human left anterior descending (LAD) coronary arteries during percutaneous transluminal coronary angioplasty (PTCA). The patients average age was $72 \pm 12$ years and six of them presented detected calcification regions and one detected soft plaque in their IVUS images. This process was approved by a local investigation review board and was performed in accordance with the ethical principles for medical research involving human subjects. We obtained written informed consent from all the subjects.

### 2.1. Fractal dimension image

The concept of fractal dimension is based on the property of self-similarity. In spite of not being self-similar over all the scales, the IVUS RF signals usually present some level of self-similarity within some range and thus the Higuchi fractal dimension can be used as an efficient method to express the irregularity of the RF signals in the ROIs of appropriate size.

Higuchi's algorithm [8] is proven to be a stable method to estimate the fractal dimension of a time series and, more importantly, works well for time series with few samples. The algorithm, computes mean length of the signal at different scales, plots a log–log graph of length versus scale and measures the slope of the linear fit of this graph as the fractal dimension.

Thus, for generation of the fractal dimension images the following algorithm was used.

**Algorithm.** For each ROI defined by the position of a 100 points wide sliding window, the following steps were used:

1. Extract the signal envelop through the calculation of the absolute value of the Hilbert transform.
2. Normalize the envelop by dividing it by its maximum value in that sample.
3. Calculate the fractal dimension of the normalized signal using the Higuchi method.
4. The sliding window is shifted of 25 points and the above steps are repeated for all RF lines that comprise the IVUS image.

### 2.2. Correlation image

Conventional B-mode IVUS images were generated from RF signals by software developed by our group [10]. Then the IVUS image was divided into $64 \times 64$ square shape ROIs. Template matching method was applied for calculation of correlation and displacement of the ROIs between the consecutive two frames. Template matching is the process of determining the presence and the location of a reference image or an object inside a scene image under analysis by a spatial cross-correlation process. Fig. 1 shows the schematic illustration of template matching method. If the coordinates of the center of the ROI in the first frame (a) are defined as $p(0,0)$ and the most similar patterned ROI in the next frame (b) is $q(k,l)$, the correlation is given by:

$$R_{fg}(k,l) = \frac{\sum_{i=0}^{n^2-1}(f_i - \bar{f}_i)(g_i - \bar{g}_i)}{\sqrt{\sum_{i=0}^{n^2-1}(f_i - \bar{f}_i)^2 \sum_{i=0}^{n^2-1}(g_i - \bar{g}_i)^2}} \quad (1)$$

where $f_i$ and $g_i$ are pixels inside the ROI in consecutive frames, $\bar{f}_i$ and $\bar{g}_i$ are the corresponding mean gray level values of each ROI, and $n$ is the length of the side of the square shaped ROI.

Please cite this article in press as: E.S. Filho et al., Fractal dimension of 40 MHz intravascular ultrasound radio ..., Ultrasonics (2007), doi:10.1016/j.ultras.2007.08.006

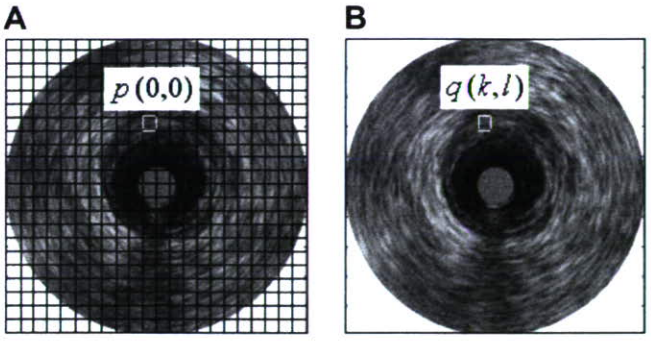


Fig. 1. Schematic illustration of template matching method. The coordinates of the center of the ROI in the first frame (A) is defined as $p(0, 0)$ and the most similar ROI in the next frame (B) is $q(k, l)$.

Based on our tests, we could observe that the moving regions such as blood and surrounding tissues presented correlation values below 0.5 and the regions of vessel wall presented correlation values above 0.75. The vessel wall was assumed stable during 1/30 s.

## 3. Results

In Fig. 2, we can see an example of two samples of IVUS RF signal extracted from the region of blood and the region of vessel wall. It can be seen that the sample extracted from the blood region presents a more irregular shape than the sample from the region of vessel. As the fractal dimension can be regarded as a measure of irregularity, we used the fractal dimension as a feature for tissue characterization.

In Fig. 3C and F, we can see two examples of fractal dimension images. They are images whose pixel colors represent the fractal dimension of a 100 points wide sliding window centered at the corresponding position in the RF line. In spite of being quite noisy, we can observe that the regions of lumen present fractal dimension values higher (light blue and green) than the vessel wall region (dark blue). More homogeneous regions, like calcification regions for example, present a lower fractal dimension value (dark blue).

Also, in Fig. 3B and E, we can compare the fractal images with the correlation images, which are images whose pixel value represents the correlation index calculated through Eq. (1). The correlation image shows its lowest level in the regions of blood (light blue), which is the most dynamic region. This fact is also detected through the fractal dimension image.

In Fig. 3A, we can observe clearly the boundary lumen/vessel that is confirmed in Fig. 3B, where the lumen region presents correlation values usually below 0.5, represented by light green or light blue, due to the fast moving blood. The red region is the static or slow moving vessel wall. In the fractal dimension image (Fig. 3C) we can observe that

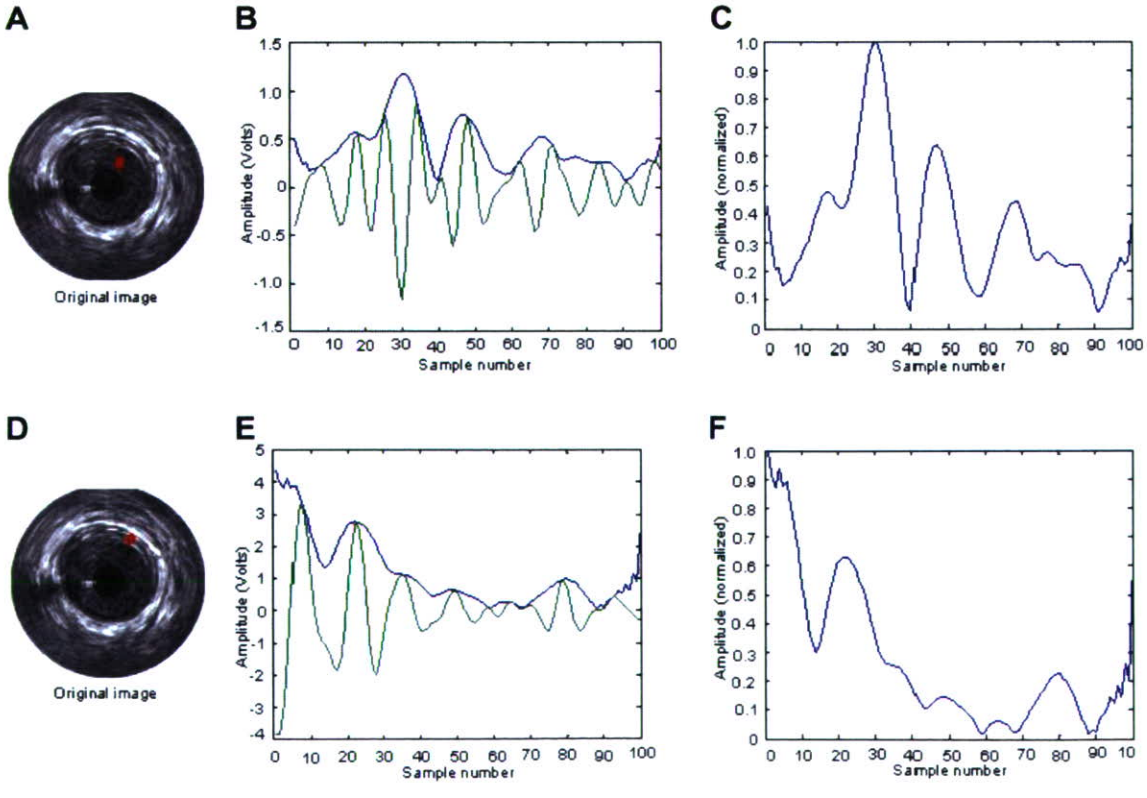


Fig. 2. Example of RF signal ROIs extracted from lumen region (A) and vessel wall region (D). The small regions in red in (A) and (D) indicate the position from where the ROIs were extracted. They are 100 samples length ROIs. (B) and (E) are the graphs of the RF signals ROIs (in green) and their respective envelop (in blue). (C) and (F) are graphs of the normalized envelops.

Please cite this article in press as: E.S. Filho et al., Fractal dimension of 40 MHz intravascular ultrasound radio ..., Ultrasonics (2007), doi:10.1016/j.ultras.2007.08.006

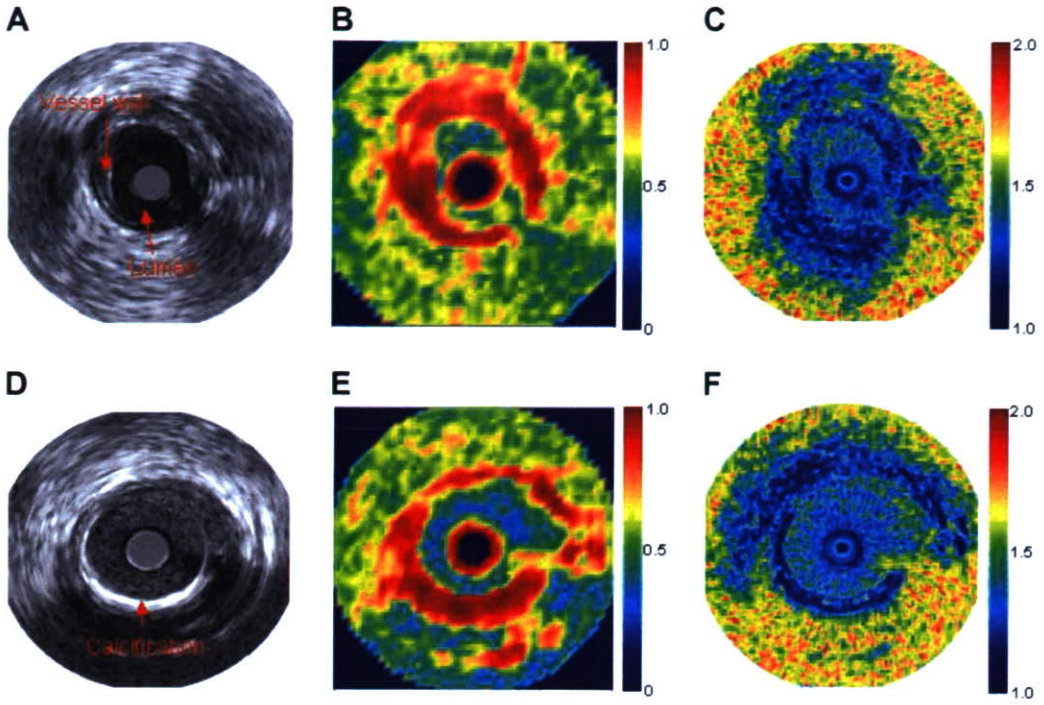


Fig. 3. Comparison between correlation image and fractal dimension image. (A) and (D) are the original images. (B) and (E) are examples of correlation images. (C) and (F) are example of fractal dimension images.

the lumen region is light blue whereas the vessel wall region is dark blue. This means that the fractal dimension in the lumen region, usually between 1.25 and 1.5, is higher than the fractal dimension in the vessel wall region that is usually below 1.20. This suggests that the irregularity level of the RF signal expressed by Higuchi fractal dimension can be used, to some extent, to characterize the moving tissues. The region outside the vessel in Fig. 3C is quite yellow and red, with fractal dimension values around 1.7, mainly because this is a region of high noise level. The corresponding area in Fig. 3B present low correlation level indicating fast moving connecting tissues. Additionally, we can observe in Fig. 3E and F that the region of calcium is also a region of high correlation value and low fractal dimension. It can also be observed that the fractal dimension images present better resolution than the correlation images.

## 4. Discussion

The examples in Fig. 2 showed that, besides the differences in amplitude, the irregularity of the envelop is fairly different in these both regions suggesting that a measure of signal irregularity could be a useful discriminator for regions of vessel wall and lumen. Saijo et al. [10] have observed similar results through the two-dimensional correlation analysis. Their results were validated by comparisons with histology data.

Accordingly to our tests, RF signal samples shorter then 60 points did not provide acceptable results because the images generated using a window of this width did not present clear contrast between the lumen and the vessel wall. The highest contrast is achieved for sliding window with width of around 100 points. Sliding windows wider than 100 points did not present visible improvements.

As reported in [8], the Higuchi method presented more stable results when compared with other methods based on power spectrum. In tests performed with IVUS RF signals the power spectrum based fractal dimension did not provide satisfactory results, probably, due to the large amount of noise, suggesting the robustness of Higuchi method.

Using the PC described in Section 2, the average processing time needed to generate the fractal dimension images was 128 s. This suggests that the proposed algorithm may be used in real time if more powerful hardware is used and the program is optimized.

The fractal dimension images presented an average contrast-to-noise ratio (CNR) of 3.73 whereas the correlation image presented 3.05. However, together with lower CNR, the correlation images present lower resolution. Thus the fractal images with a CNR of 3.05 seen to present a satisfactory trade-off between noise and resolution because the resultant fractal dimension images presented less distortion of the lumen contour than the correlation images as can be seen in Fig. 3.

Comparing images from different patients, for example, patients with calcification and patients without calcification, we could observe that the fractal dimension values in the calcification regions is similar to levels presented in the vessel wall region, as shown in Fig. 3. This

Please cite this article in press as: E.S. Filho et al., Fractal dimension of 40 MHz intravascular ultrasound radio ..., Ultrasonics (2007), doi:10.1016/j.ultras.2007.08.006

suggests that the fractal dimension images may not be useful in calcification detection. In tests with image containing soft plaque, the resulting fractal dimension image did not present clear contrast between the soft plaque and blood. Thus, this method does not seem likely to be a good discriminator for plaques. However, it may be useful as a pre-processing stage toward luminal contour detection.

## 5. Conclusion

A comparison between correlation images and fractal dimension images was presented and we could observe that, in general, the regions of high correlation values in the correlation image correspond to the regions of low fractal dimension in the corresponding fractal dimension image and vice-versa. This fact suggests that the fractal dimension, as measure of irregularity of the RF echo signal, can be also an indicator of the moving characteristic of the interrogated tissue as well as the correlation image. However, the fractal dimension image has the advantage of presenting more clearly the fine details of the luminal contour when compared to the correlation images.

## Acknowledgement

This study was supported by the Grants-in-Aid from the Ministry of Health, Labor and Welfare of Japan (H17-nano-001).

## References

[1] A. Nair, B.D. Kuban, N. Obuchowski, D.G. Vince, Assessing spectral algorithms to predict atherosclerotic plaque composition with normalized and raw intravascular ultrasound data, Ultrasound in Medicine and Biology 27 (2001) 1319–1331.

[2] R. Jennane, W.J. Ohley, S. Majumdar, G. Lemineur, Fractal analysis of bone X-ray tomographic microscopy projections, IEEE Transactions on Medical Imaging 20 (2001) 443–449.

[3] T. Stosic, B.D. Stosic, Multifractal analysis of human retinal vessels, IEEE Transactions on Medical Imaging 25 (2006) 1101–1107.

[4] P. Asvestas, S. Golemati, G.K. Matsopoulos, K.S. Nikita, A.N. Nicolaides, Fractal dimension estimation of carotid atherosclerotic plaques from b-mode ultrasound: a pilot study, Ultrasound in Medicine and Biology 28 (2002) 1129–1136.

[5] W.L. Lee, Y.C. Chen, K.S. Hsieh, Ultrasonic liver tissues classification by fractal feature vector based on m-band wavelet transform, IEEE Transaction on Medical Imaging 22 (2003) 382–392.

[6] B. Alacam, B. Yazici, N. Bilgutay, F. Forsberg, C. Piccoli, Breast tissue characterization using modeling of ultrasonic RF echo, Ultrasound in Medicine and Biology 30 (2004) 1397–1407.

[7] M. Moradi, P. Ablmaesumi, P.A. Isolato, D.R. Siemens, E.E. Sauerbrei, P. Mousavi. A new feature for detection of prostate cancer based in RF ultrasound echo signals, in: Proceedings of IEEE Ultrasonics Symposium, 2006. pp. 2084–2087.

[8] T. Higuchi, Approach to an irregular time series on the basis of the fractal theory, Physica D 31 (1988) 277–283.

[9] R.M. Rangayyan, Biomedical Image Analysis, CRC Press, Boca Raton, FL, USA, 2005, pp. 1118.

[10] Y. Saijo, A. Tanaka, T. Iwamoto, E. Santos Filho, M. Yoshizawa, A. Hirosaka, M. Kijima, Y. Akino, Y. Hanadate, T. Yambe, Intravascular two-dimensional tissue strain imaging, Ultrasonics 44 (2006) e147–e151.

[11] Y. Saijo, A. Tanaka, N. Owada, Y. Akino, S. Nitta, Tissue velocity imaging of coronary artery by rotating-type intravascular ultrasound, Ultrasonics 42 (2004) 753–757.

Please cite this article in press as: E.S. Filho et al., Fractal dimension of 40 MHz intravascular ultrasound radio ..., Ultrasonics (2007), doi:10.1016/j.ultras.2007.08.006